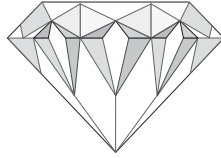


Diploma Thesis



Diamond Detectors for Ionizing Radiation

University of Technology, Vienna

Committee:

Univ. Prof. Dr. Wolfgang Fallmann

Institute of Applied Electronics and Quantum Electronics, University of Technology Vienna

Univ. Prof. Dr. Meinhard Regler

Institute of High Energy Physics, Austrian Academy of Sciences

Markus Friedl

Belvederegasse 19/8

A-1040 Vienna

Markus.Friedl@cern.ch

January 1999

Electronically available at <http://wwwhephy.oeaw.ac.at/u3w/f/friedl/www/da/>

Contents

1	Synopsis	4
2	Introduction	6
3	Material Properties	9
3.1	General Properties	9
3.2	Electrical Properties	10
3.3	Types of Diamond	11
3.4	CVD Process	11
4	Solid State Detector Theory	15
4.1	Bethe-Bloch Theory	15
4.2	Landau Distribution	16
4.3	Principal Detector Layout	18
5	Detector Material Comparison	20
5.1	Diamond Detectors	20
5.1.1	Charge Collection Distance	20
5.1.2	Collection Distance vs. Electric Field	22
5.2	Si Detectors	23
5.3	Ge Detectors	25
5.4	GaAs Detectors	25
6	Characterization	26
6.1	Characterization Setup	26
6.1.1	Particle Source	27
6.1.2	Detector Amplifiers	27
6.1.2.1	Charge-Sensitive Amplifier	28
6.1.2.2	Grounded Base Amplifier	29
6.1.3	Readout Electronics	30
6.1.4	Data Acquisition Software	31
6.2	Calibration and Noise Measurements	32
6.3	Fit Model	33

7	Radiation Hardness	37
7.1	Radiation Defects	37
7.2	Pumping Effect	38
7.3	Irradiation	39
7.3.1	Pion Irradiation	39
7.3.1.1	Collection Distance	40
7.3.1.2	Beam Induced Charge	41
7.3.2	Electron Irradiation	43
7.3.3	Photon Irradiation	43
7.3.4	Proton Irradiation	44
7.3.5	Neutron Irradiation	44
7.3.6	Alpha Irradiation	45
7.4	Comparison	45
8	Detector Geometries	48
8.1	Dots	48
8.2	Strips	49
8.2.1	Spatial Resolution	49
8.2.2	Measurements	50
8.3	Pixels	52
9	Summary	55
	Acknowledgements	57
	Appendix	
A	Abbreviations and Symbols	58
B	My Work with Diamonds	62
	Bibliography	63

Chapter 1

Synopsis

Diamonds are a girl's best friend.

M. Monroe

In fact, diamonds are more than that. Widely known for its hardness, industrial diamond has been successfully applied to drilling and cutting tools all over the world. However, artificially grown diamond can also serve for particle detection, similar to semiconductors such as silicon or germanium. Due to its expected radiation hardness, diamond is a candidate for future high energy experiments.

The RD42 collaboration at CERN (European Laboratory for Particle Physics, Geneva, CH) has been installed in 1994 to develop diamond detectors and readout electronics for the experiments at the Large Hadron Collider (LHC), which is planned to start running in 2005. The projected features of this machine will exceed the limits of present technology in many fields. In the past years, several institutes joined the RD42 collaboration, which has now approximately 80 scientific members from 24 institutes all over the world.

In 1995, I began to work with the HEPHY [1] (Institute of High Energy Physics, Vienna, A) of the Austrian Academy of Sciences. Soon I got in touch with diamond detectors and became a member of the RD42 collaboration. In 1995, we built a characterization station for solid state detector samples, especially diamonds. It took quite a lot of time to understand and optimize the device, as we developed almost everything from scratch, from the mechanical support to the software. I laid special emphasis on achieving the lowest noise possible in the design of this characterization station. In the autumns of 1995, 1996 and 1997, we performed three irradiation experiments in a pion beam at the Paul Scherrer Institute (PSI, Villigen, CH). Because of my essential contribution to preparation, realization and data analysis, ample space is devoted to these projects within this thesis. Also numeric calculation of electric fields was included in my further analysis. A summary of my personal “diamond career” is given in appendix B.

This thesis is divided into several chapters, each of which deals with a certain aspect of diamond detectors. A general introduction and the motivation for diamond detector research is given in chapter 2. The growth and properties of diamond are described in chapter 3, while chapter 4 gives a brief overview of the theoretical background of particle detection. Under this aspect, diamond is compared to other solid state detector materials,

primarily silicon, in chapter 5. The characterization of diamond detectors is dealt with in chapter 6. In chapter 7, the radiation hardness studies are described with emphasis on the pion irradiation. The various detector geometries, including the latest test results of strip and pixel detectors, are dealt with in chapter 8. Finally, chapter 9 summarizes the results which have been achieved. Abbreviations and symbols are explained in appendix A.

As the study of diamond detectors for the application in future high energy experiments has begun only in the 1990s, I am restricted to discuss the present state of investigations. Up to now, more than 150 diamond samples have been investigated by the RD42 collaboration. The results look very promising and I expect that diamond detectors may be widely used in future applications. The latest results, all RD42 publications as well as several photos and figures can be obtained at <http://www.cern.ch/RD42/> .

Chapter 2

Introduction

Diamond is a material with a set of very unique characteristics. It is mainly known as a gem, but also for its hardness. There is a third property that is not so well known; diamond shows extremely high thermal conductivity while it is electrically insulating.

Besides that, diamond has the reputation of being radiation hard since the 1950s, but only recently this has been examined systematically using modern irradiation facilities. One field of future applications of CVD (chemical vapor deposition) diamond could be particle detection in high energy physics experiments, where fast, radiation-hard detectors are required.

The goal of the RD42 collaboration is the development of tracking detectors¹ made of CVD diamond for the LHC. The group is involved in both the ATLAS (A Toroidal LHC Apparatus) and the CMS (Compact Muon Solenoid) experiments, which are projected for the LHC. As I am affiliated with CMS, I will give a short description of the possible utilization of diamond there.

Fig. 2.1 shows the complete CMS experiment. Only the pink cylinder in the very center is the solid state tracking detector, containing strip and pixel detectors. While the strip detectors will be definitely made of silicon, the material for the pixel detectors could be either silicon or diamond.

The reason for this diamond option is the extreme radiation in the vertex environment. Present standard silicon detectors are operable up to a fluence of approximately 10^{14} particles cm^{-2} [2]. With this fluence, the radiation defects do no longer allow meaningful measurements. The total fluences of photons, neutrons and charged hadrons expected in the CMS experiment over the scheduled 10 years of LHC operation is shown in fig. 2.2. z is the distance from the vertex along the beam axis, while the parameter r is the radius from the beam axis.

Two permanent pixel layers are planned at radii of 7 and 11 cm and a third one at $r = 4$ cm only for the low luminosity period in the beginning of LHC operation. The photon and neutron fluences are silicon-compliant. The charged hadrons, however, most of which are pions with a momentum below $1 \text{ GeV } c^{-1}$, are a challenge, which can be accomplished with diamond detectors.

¹position-sensitive detectors with good spatial resolution

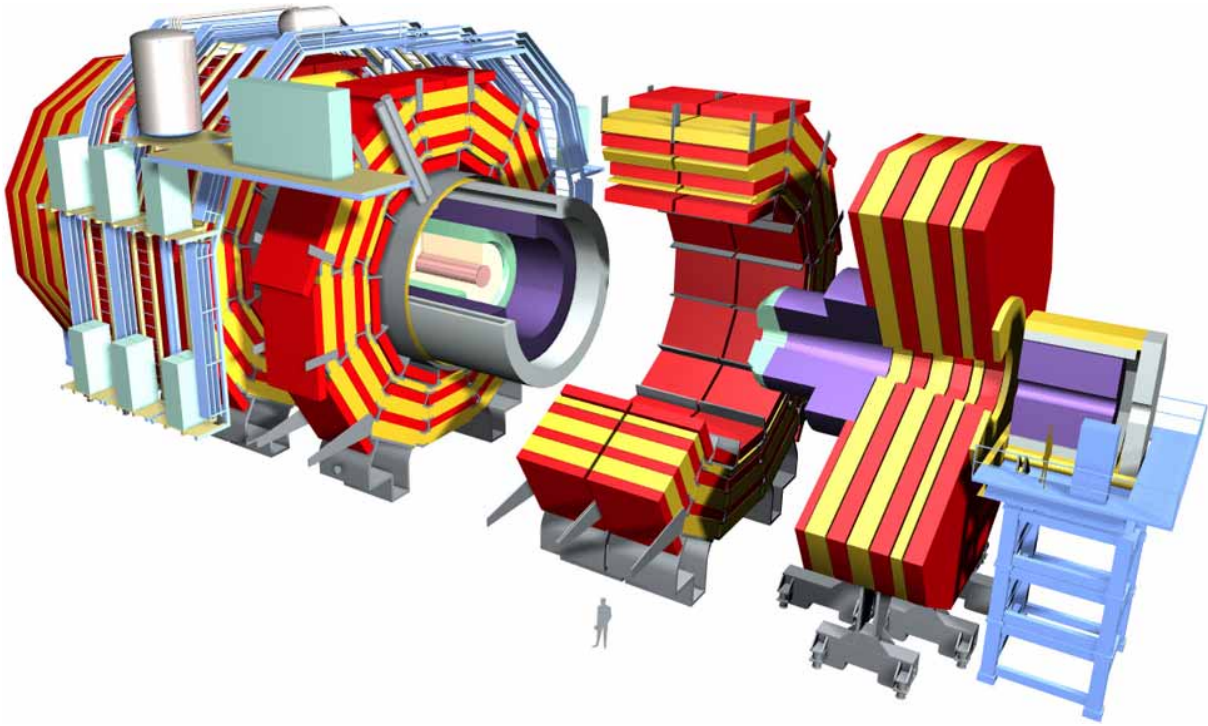


Figure 2.1: The CMS experiment at CERN.

Not only the LHC groups are interested in CVD diamond. Proposals have been submitted for using CVD diamond detectors for monitoring of heavy ion beams at GSI-Darmstadt [4] and for a research program for a vertex detector upgrade at Fermilab [5].

Besides the narrow field of high energy physics, one can imagine to produce semiconductor devices based on diamond. However, presently there is one major technical restriction. While intrinsic diamond is easily engineered to a p-type semiconductor by implantation of boron acceptors, no reasonable donor material has been found yet.

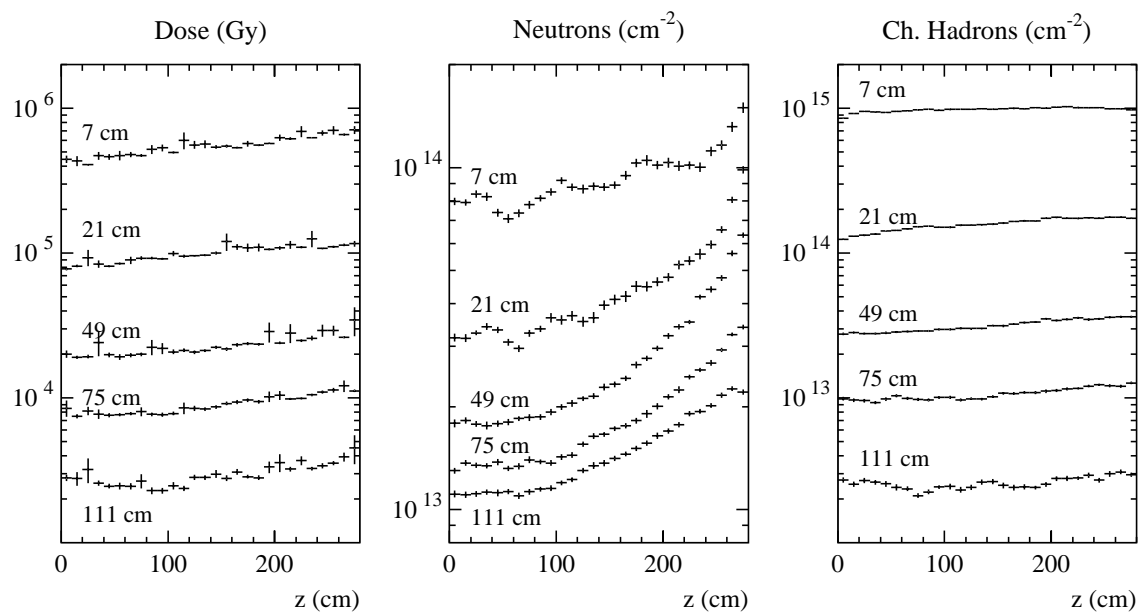


Figure 2.2: The expected radiation fluences of photons, neutrons and charged hadrons in the CMS experiment over 10 years of operation. [3]

Chapter 3

Material Properties

3.1 General Properties

Diamond is composed of carbon atoms arranged in the tetrahedron diamond lattice (fig. 3.1). The atoms stick together through strong sp^3 σ -type bonds. The small carbon atoms give a very dense, but low weight lattice. These facts give reason for the extraordinary characteristics of diamond.

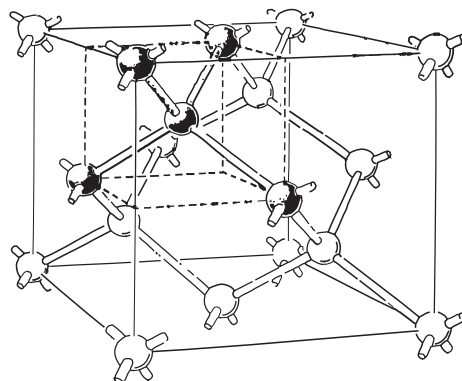


Figure 3.1: The diamond lattice [6].

Quantity	Value	Applications
Refraction index n (at $\lambda = 550$ nm)	2.42	Gem
Hardness (after MOHS ¹)	10	Drills, Cutters
Thermal conductivity σ_T [$W\ cm^{-1}\ K^{-1}$]	20	Heat Sink

Table 3.1: Some outstanding features of diamond.

¹FRIEDRICH MOHS, *1773 in Gernrode, †1839 in Agordo, Austrian mineralogist who devised a hardness scale for minerals in 1812.

Tab. 3.1 lists some outstanding features of diamond material. The refraction index, which is quite high for an optically transparent material, together with special cutting, e.g., the brilliant type, gives reason for a number of total reflections and diffraction of white light on its long path through the diamond. This leads to the sparkling of the gems, well known by everyone. Glass imitations show less sparkling, because the refraction index of glass is only about $n = 1.5$, reducing the angle range where total reflection occurs. Thus the path length of the light is shorter, which gives less opportunity for diffraction.

Diamond is the hardest mineral known, therefore it is used for drilling and cutting applications. One really wonders how diamond itself is cut... The answer, of course, is: with another diamond, mechanically enforced by fast rotation, or, more recently, by a laser.

The thermal conductivity of diamond is the highest of any material known; at room temperature it is five times higher than that of copper. Even more, it is coupled with electrical insulation, which is a very rare combination in nature. Specially treated synthetic diamond crystals conduct heat even better, a value of $33 \text{ W cm}^{-1} \text{ K}^{-1}$ has been reported [7]. Therefore, diamond heatsinks are used, e.g., in Pentium Processors, where a huge amount of thermal power has to be dissipated in a very small volume.

3.2 Electrical Properties

For the detector application mainly electrical properties are of interest, along with some atom related figures. Tab. 3.2 shows the properties [6, 7, 8, 9, 10] of diamond, silicon, germanium and gallium arsenide, all of which are candidates for solid state radiation detectors. The features of the materials can be compared using this table. To start with the advantages of diamond, the low atomic number minimizes particle scattering and absorption, a property which is desirable for a tracking detector. The radiation length, stating the mean distance over which a high-energy electron loses all but e^{-1} of its energy by bremsstrahlung, also scales with the inverse variance of the Coulomb scattering angle. Thus, the angle spread per unit length is slightly smaller in diamond compared to silicon. Furthermore, the high band gap, causing the low intrinsic carrier density and thus the extremely high resistivity (or negligible dark current), allows detector operation without a pn-junction, i.e., without depletion by a reverse bias voltage, unlike the other materials. The high carrier mobilities give reason for fast signal collection. Finally, the low dielectric constant implies low capacitive load of the detector and thus, together with the negligible dark current, a lower noise figure.

There is only one major disadvantage with diamond, its low signal output, which has two reasons. Due to the large band gap, the ionization, or more exact, electron-hole generation, is significantly smaller compared to the other materials. Secondly, the charge collection efficiency is quite low, caused by the polycrystalline structure of CVD diamond (this will be discussed in detail in section 5.1.1).

Perhaps the most important characteristic of diamond as a new detector material is its hardness against all types of radiation, which is described in chapter 7.

Quantity	Diamond	Si	Ge	GaAs
Atomic number Z	6	14	32	31, 33
Number of atoms N [10^{22} cm^{-3}]	17.7	4.96	4.41	4.43
Mass density ρ [g cm^{-3}]	3.51	2.33	5.33	5.32
Radiation length X_0 [cm]	12.0	9.4	2.3	2.3
Relative dielectric constant ϵ	5.7	11.9	16.3	13.1
Band gap E_g [eV]	5.47	1.12	0.67	1.42
Intrinsic carrier density n_i [cm^{-3}]	$< 10^3$	1.45×10^{10}	2.4×10^{13}	1.79×10^6
Resistivity ρ_c [$\Omega \text{ cm}$]	$> 10^{12}$	2.3×10^5	47	10^8
Electron mobility μ_e [$\text{cm}^2 \text{ V}^{-1} \text{ s}^{-1}$]	1800	1350	3900	8500
Hole mobility μ_h [$\text{cm}^2 \text{ V}^{-1} \text{ s}^{-1}$]	1200	480	1900	400
Saturation field E_s [V cm^{-1}]	2×10^4	2×10^4	2000	3000
Electron saturation velocity v_s [10^6 cm s^{-1}]	22	8.2	5.9	8.0
Operational field E_o [V cm^{-1}]	10^4	2000	1000	2000
Electron operational velocity v_o [10^6 cm s^{-1}]	20	3	3	10
Energy to create e-h pair E_{eh} [eV]	13	3.6	3.0 (@77K)	4.3
Mean MIP ionization q_p [$\text{e } \mu\text{m}^{-1}$]	36	108	340	130

Table 3.2: The properties of solid state detector materials at $T = 300 \text{ K}$.

3.3 Types of Diamond

In the early 20th century, natural diamonds were divided into type I, containing nitrogen impurities, and type II, relatively free of nitrogen. Later, by refining the analysis methods, subgroups were introduced to the type terminology as shown in tab. 3.3. Natural diamond,

Type	Impurities	Comments
Ia	Aggregated nitrogen up to 2500 ppm	Most natural diamonds
Ib	Substitutional nitrogen up to 300 ppm	Most synthetic diamonds
IIa	Substitutional nitrogen < 1 ppm	Detector material
IIb	Boron doped	p-type semiconductor

Table 3.3: The diamond type terminology.

which is found mainly as type Ia, is not applicable as a detector because of its nitrogen impurities. Reasonable detector material, synthesized in the CVD process, must contain less than 1 ppm of nitrogen (type IIa). With natural or synthetic boron implantation, p-type semiconducting behavior is introduced to the material.

3.4 CVD Process

Diamond detectors are grown in the chemical vapor deposition (CVD) process. A small fraction of hydrocarbon gas, such as methane, is mixed with molecular hydrogen and

oxygen gas. When the gas mixture is ionized, carbon based radicals are reduced and settle on a substrate, usually silicon or molybdenum, and link together with σ -type bonds, forming a diamond lattice. Successful diamond deposition is restricted to a well defined area within the C-H-O ternary diagram shown in fig. 3.2. Outside this area, either non-diamond carbon or nothing at all is grown.

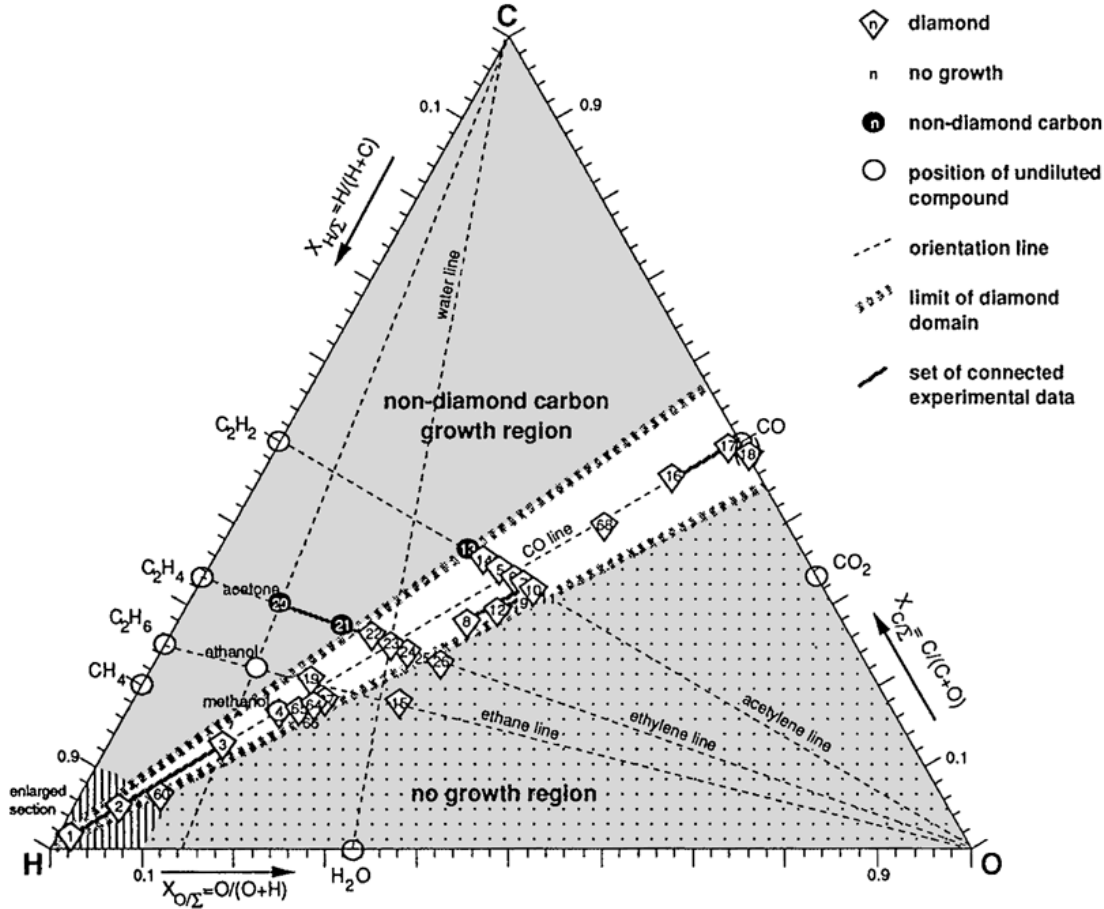


Figure 3.2: The C-H-O ternary diagram. CVD Diamond growth is restricted to the white area in the center [7].

The properties of the diamond grown in this process depend on the gas mixture, temperature and pressure. Although this is an easy principle, the growth process is extremely difficult to control in order to grow material suitable for detector application; the parameters are not constant throughout the process. The growth speed is typically about $1 \mu\text{m h}^{-1}$. There are several types of CVD reactors, which differ in the way the gas is ionized; e.g., this is done by microwaves or by a heating wire. After the growth process, the substrate is etched from the diamond film, which is then cut and cleaned.

Initially, there is a large number of small crystal seeds on the substrate, each oriented individually. As deposition continues, the grains grow together, forming columnar single-crystals with grain boundaries between. On the substrate side the lateral grain size is very small (in the order of micrometers), while the size continuously increases in the growth

direction, reaching a diameter in the order of $100\ \mu\text{m}$ with a diamond film thickness of $500\ \mu\text{m}$. The section of a CVD grown diamond, visualizing this “cone”-like structure is shown schematically in fig. 3.3 and as a SEM (scanning electron microscopy) photograph in fig. 3.4.

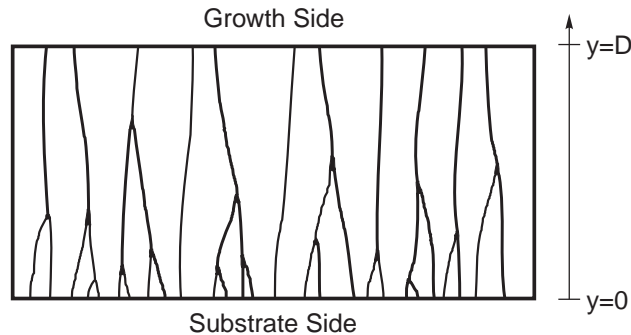


Figure 3.3: Schematic section of a diamond film.

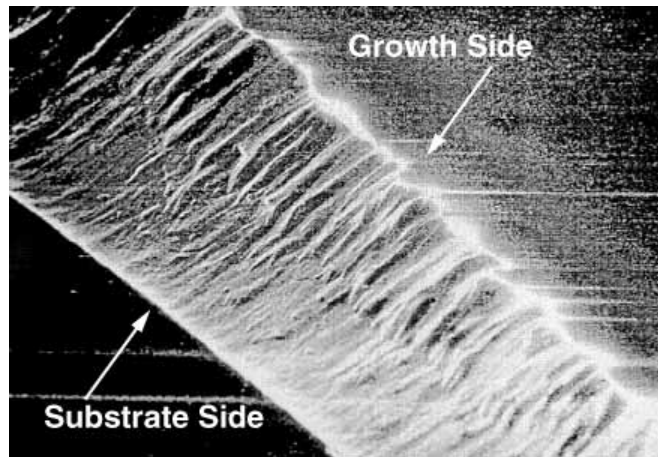


Figure 3.4: Photograph of the section of a diamond film.

The different grain sizes of substrate and growth sides are clearly visible with the SEM photographs in fig. 3.5. The grain size expands from approximately $2\ \mu\text{m}$ at the substrate side ($y = 0$) to about $80\ \mu\text{m}$ at the growth side ($y = 415\ \mu\text{m}$).

The CVD diamond samples used by the RD42 collaboration have been grown by the commercial manufacturers St. Gobain/Norton [11] and De Beers [12]. Most of the samples were grown on 4" wafers in a research reactor and then laser cut into $1 \times 1\ \text{cm}^2$ pieces. Recently, several $2 \times 4\ \text{cm}^2$ samples were delivered from a production reactor. The as-grown thickness of the CVD samples ranges from $300\ \mu\text{m}$ up to almost 3 mm.

For the detector application, the diamond film is equipped with contacts on either side. First a chromium layer of typically 50 nm is sputtered onto the sample, which forms a carbide with the diamond, providing an Ohmic contact. Then, a gold layer (typically

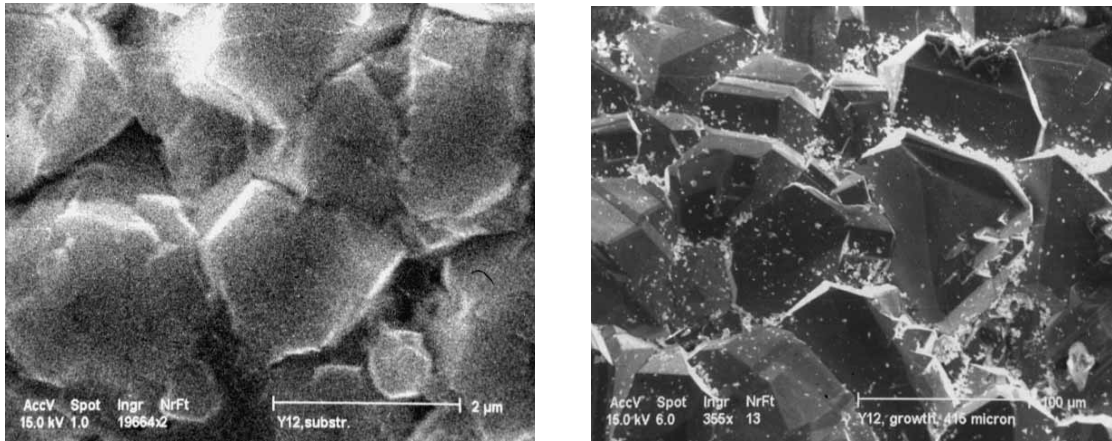


Figure 3.5: Left: Substrate (left) and growth (right) sides of the same diamond sample ($415 \mu\text{m}$ thick). Note the different scales of the images: $2 \mu\text{m}$ for the substrate side and $100 \mu\text{m}$ for the growth side.

200 nm) is sputtered to prevent oxidation and to provide a surface suitable for wire-bonding. Besides this standard contact, also a Ti/Au combination was used. For the indium bump bonding of pixel detectors (see section 8.3), Cr/Ni/Au and Ti/W processes were developed.

Chapter 4

Solid State Detector Theory

When a heavy charged particle traverses material, energy is mainly transferred due to Coulomb interactions between the particle and the atomic electrons in the material. In solids with an atomic lattice, which can be described by the band model, the electrons are excited from the valence to the conduction band when the particle transfers enough energy. This process is known as electron-hole generation. At very high incident particle energies, also radiation is emitted when collisions occur, which is called bremsstrahlung.

4.1 Bethe-Bloch Theory

H.A. BETHE¹ and F. BLOCH² developed a theory based on energy and momentum conservation for the energy loss of charged particles other than electrons at high energies ($v \approx c$) traversing material, stated in terms of dE/dx , when radiative energy loss is negligible [13, 14].

$$-\frac{1}{\rho} \frac{dE}{dx} = 4\pi N_A r_e^2 m_e c^2 z^2 \frac{Z}{A} \frac{1}{\beta^2} \left[\frac{1}{2} \ln \left(\frac{2m_e c^2 \beta^2 \gamma^2 T_{\max}}{I^2} \right) - \beta^2 - \frac{\delta(\gamma)}{2} \right] \quad (4.1)$$

Eq. 4.1 represents the differential energy loss per mass surface density [$\text{MeV} (\text{g cm}^{-2})^{-1}$], where ze is the charge of the incident particle, N_A , Z and A are Avogadro's number, the atomic number and the atomic mass of the material, m_e and r_e are the electron mass and its classical radius ($\frac{e^2}{4\pi\epsilon_0 m_e c^2}$). T_{\max} is the maximum kinetic energy which is still detected in the material, I is the mean excitation energy, $\beta = v/c$, $\gamma = (1 - \beta^2)^{-1/2}$ and $\delta(\gamma)$ is a correction for the shielding of the particle's electric field by the atomic electrons, the density effect caused by atomic polarization.

For $0.1 < \beta\gamma < 1.0$, the dE/dx curves (fig. 4.1) approximately fall proportionally to β^{-2} , then show a broad minimum at $\beta\gamma = 3$ to 4 (decreasing with Z) and finally slowly

¹HANS ALBRECHT BETHE, *1906 in Strasbourg. Most of the time he worked with the Cornell University, interrupted by sabbaticals leading him to CERN and other research centers. For his contributions to the theory of nuclear reactions he was awarded the Nobel Prize in 1967.

²FELIX BLOCH, *1905 in Zurich, †1983. He was working with a number of universities and research centers, like Stanford and CERN. The Nobel Prize was awarded to him in 1952 for nuclear magnetic precision measurements.

rise with higher energies. This is known as relativistic rise. A heavy charged particle

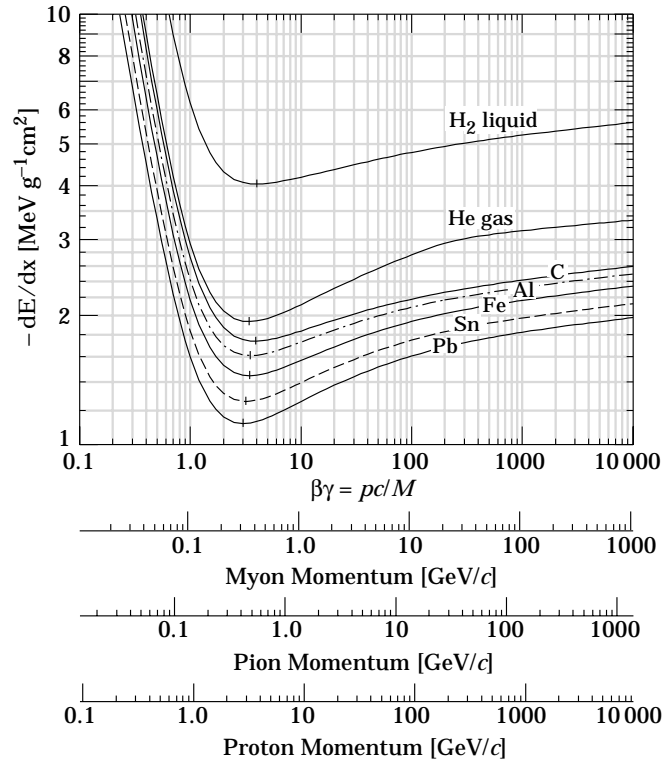


Figure 4.1: Energy loss (dE/dx) curves for various materials [13].

with an energy in the minimum of the dE/dx curve deposits the least amount of energy possible; it is therefore called MIP (minimum ionizing particle).

Uncharged particles do not show any interaction within the Bethe-Bloch theory, only secondary reactions involve Coulomb forces. In fact, the energy deposit is smaller by orders of magnitude, which has been shown, e.g., with the neutron irradiation of diamond [15].

4.2 Landau Distribution

Particles that are stopped in a thick layer of material transfer their whole energy to the bulk. The mean range of these particles can be obtained by integration of eq. 4.1. Due to fluctuations, the effective range spectrum is of Gaussian shape.

In the case of thin layers, when the particle traverses the material, the deposited energy is only a small fraction of the incident particle energy. Furthermore, excited δ electrons³ may leave the bulk. The Bethe-Bloch formula must be adapted to this case by applying certain cuts [16, 17]. This implies that the relativistic rise ends up by a plateau due to the compensation of the remaining relativistic rise by the energy dependence of the shielding

³electrons receiving a large amount of energy from a heavy collision with the incident particle, also referred to as “knock-on electrons”

effect in the highly relativistic domain. Moreover, the dE/dx minimum shifts to higher energies. Thus, for practical reasons, all particles with energies above the MIP energy are considered as approximately minimum ionizing in solid state detectors.

The energy spectrum observed in thin layers was described by L.D. LANDAU⁴ [18]. It resembles a Gaussian distribution with a long upper tail, resulting from a small number of δ electrons, which have experienced a large energy transfer from the primary particle. This energy is deposited by a subsequent cascade. The exact analytic notation of the Landau distribution is an inverse Laplace transform,

$$L(x) = \mathcal{L}^{-1} s^s \quad (4.2)$$

Several approximations exist, the simplest way is to use the Gaussian function, if the intention is to fit at the most probable (peak) region only. J.E. MOYAL states an “explicit expression of Landau’s distribution” [19], given in eq. 4.3, which in fact is only an approximation.

$$L(x) \approx P_4 \exp \left[-\frac{1}{2} (A + e^{-A}) \right] \quad (4.3)$$

$$A = P_3 \frac{P_1 + x}{P_2 - P_1}$$

The approximation by K.S. KÖLBIG and B. SCHORR [20] is part of the CERN Computer Center Program Library [21]. Using basically a piecewise polynomial approximation, an accuracy of at least seven digits is ensured. Fig. 4.2 shows the exact (numerically integrated) Landau distribution and the two approximations mentioned above.

The Landau distribution is an approximation for particles traversing thin layers of material, which agrees well with the observed spectra. Its limit is the long tail, which theoretically extends to infinite energies, while the energy deposited by an incoming particle cannot exceed its own energy. The convolution of two Landau distributions results in another Landau distribution. This property can be illustrated by the energy loss of a particle traversing a layer of thickness D or two subsequent layers of thickness $\frac{D}{2}$, respectively. The overall energy loss must be the same in both cases, implying the convolution property mentioned above. The Landau distribution has a finite area, however, it is impossible to state a mean value or moments of higher order. One possible workaround is to cut the Landau tail, which implies the loss of the convolution property. The method we used, which is closer related to the measured spectrum data, will be discussed in section 6.3.

Protons, pions and other types of charged particles, which are in most cases close to MIPs, all produce approximately Landau-distributed spectra when traversing diamond film. Electrons from a beta source are also close to minimum ionizing when low energetic particles (β^{-2} range) are excluded, as discussed in section 6.1.1. Alpha particles, i.e., He nuclei, however, are stopped in diamond after a few ten micrometers, and therefore transfer all their energy on to the diamond bulk, delivering much higher, Gaussian-distributed signals than MIPs do.

⁴LEV DAVIDOVICH LANDAU, *1908 in Baku, †1968 in Moscow. The work of the Soviet physicist covers all branches of theoretical physics. In 1962 the Nobel Prize was awarded to him for his pioneering theories about condensed matter, especially liquid helium.

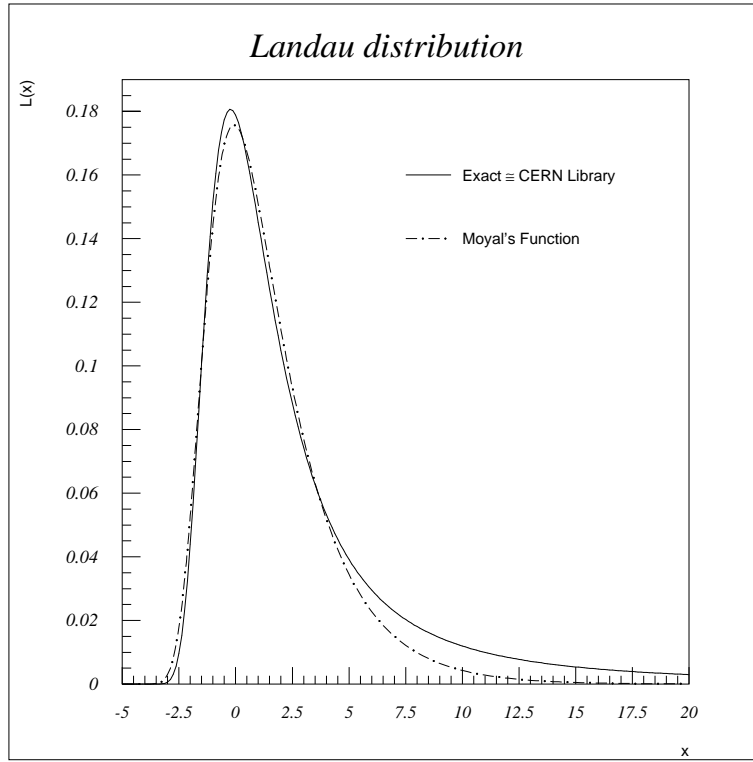


Figure 4.2: The exact Landau distribution, which is covered by the CERN Library approximation in this plot, and Moyal's approximation.

4.3 Principal Detector Layout

Most solid state detectors are made for particle tracking. Thus, the absolute signal value is irrelevant in most cases. However, as the signal coming from a MIP traversing the detectors is only in the order of several thousand electrons, one aims to maximize the signal-to-noise ratio (SNR). While the signal size depends on the detector material and geometry, the amplifier usually dominates the noise figure.

In order to minimize particle scattering and absorption, tracking detectors are made of thin layers of material, usually in the order of a few hundred micrometers, with electrodes on opposite sides to apply the “bias” voltage and drain the particle induced signal. One electrode can be formed as strips or pixels to obtain position information, as discussed in chapter 8. Nevertheless, for a simple model we will assume pad contacts.

Fig. 4.3 shows the detector function, which is in principal a charge movement inside a capacitor.

In the band model, the number of charges in the conduction band per unit volume at equilibrium, called intrinsic carrier density n_i , is given by

$$\begin{aligned} n_i^2 &= N_C N_V e^{-\frac{E_g}{kT}} \quad , \\ N_{C,V} &= \frac{2}{h^3} \left(2\pi m_{e,h}^* kT \right)^{\frac{3}{2}} \quad . \end{aligned} \quad (4.4)$$

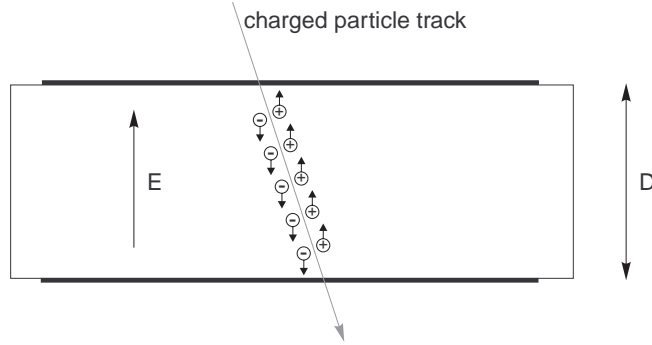


Figure 4.3: A charged particle traversing the detector generates electron-hole pairs along its track.

N_C and N_V are the weights of conduction and valence bands, E_g is the band gap, k the Boltzmann constant, T the absolute temperature, h is the Planck constant, m_e^* and m_h^* are the effective masses of electrons and holes, respectively. The intrinsic carrier density strongly depends on the band gap and the temperature. Materials with a low band gap, implying a large number of intrinsic carriers, need either cooling down to temperatures where the carriers are no longer excited or a reverse-biased pn-junction, which results in a space charge zone free of carriers.

Initially, all free carriers inside the bulk are drained by the applied electric field. There is no charge movement in the bulk, except for thermally excited electron-hole pairs, which immediately drift to the electrodes.

When a charged particle traverses the detector, electron-hole pairs are created along the particle track. In the case of a MIP perpendicularly traversing a detector of thickness D , the number of generated pairs is $Q_p = q_p D$. The electrons move towards the positive electrode, while the holes drift in the opposite direction. As these carriers move, a charge is induced at the electrodes, which can be observed by a charge-sensitive amplifier, or, in the case of high particle rates, measured as a DC current in the bias line. It is irrelevant whether the generated charges finally reach the electrodes or not, only the length of their path contributes to the (integral) signal. Especially when trapping or recombination occurs (as in CVD diamond), many charges do not reach the electrodes.

Seen from the point of a subsequent amplifier, the detector is electrically represented by a (pulse) current source in parallel to a capacitance (fig. 4.4).

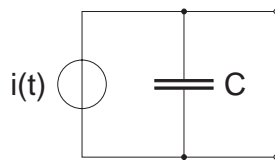


Figure 4.4: The electric representation of a detector, a current source in parallel to a capacitance.

Chapter 5

Detector Material Comparison

5.1 Diamond Detectors

With a band gap of $E_g = 5.5\text{eV}$, diamond is regarded as an insulator. This implies negligible intrinsic carrier densities even at room temperature, allowing to operate intrinsic diamond film as a detector. Electrodes are applied to the diamond film on opposite sides to form Ohmic contacts. As there is no pn-junction, the polarity of the electric field is irrelevant. The dark current of the diamond samples, including both bulk and surface currents, is less than 1 nA cm^{-2} at an electric field of $1\text{ V }\mu\text{m}^{-1}$ [22].

According to the high carrier mobilities in diamond, the charge collection is very fast, taking about 1 ns in detectors of approximately $500\text{ }\mu\text{m}$ thickness. It has been shown that CVD diamond detectors are able to count heavy ion rates above $10^8\text{ cm}^{-2}\text{ s}^{-1}$ with a single readout channel.

5.1.1 Charge Collection Distance

Due to the polycrystalline nature of CVD diamond, the charge collection is not straightforward as in homogeneous detector materials. The grain structure (fig. 3.3) results in a quality gradient along the y coordinate (depth axis). The grain boundaries are suspected to provide charge trapping and recombination centers.

On the substrate side ($y = 0$), the lateral grain size is at its minimum, resulting in a large amount of traps. Thus, the mean free path for the carriers is very short. With ascending y the single-crystal volumes expand, causing the trap density to shrink and the mean free path to increase. A linear model has been proposed [23] for the local mean free path as a function of y , starting from (almost) zero at $y = 0$ up to a certain value for $y = D$. This model satisfies experimental data [24].

Neglecting border limits, the sum of the mean free paths for electrons and holes gives the overall average distance that electrons and holes drift apart in an electric field. This value has been established as the *charge collection distance* d_c , describing the quality of the diamond sample. The border limits are irrelevant as long as $d_c \ll D$. The collection distance, or sum mean free path, can be stated as the product of carrier velocity and

lifetime, summed for both carriers,

$$d_c = d_{c,e} + d_{c,h} = v_e \tau_e + v_h \tau_h = (\mu_e \tau_e + \mu_h \tau_h) E \quad . \quad (5.1)$$

Taking the border limits into account, the collection distance obtained from measurements is smaller than the average mean free path because at the electrodes, electrons and holes are drained and do no longer contribute to the drift path, thus reducing the total drift length or the signal induced at the electrodes, respectively.

The number of charges (electron-hole pairs) generated by a MIP is [8]

$$Q_p = q_p D \quad \text{with } q_p = 36 \text{ e } \mu\text{m}^{-1} \quad . \quad (5.2)$$

The value of q_p includes not only the primary excitation, but also the contribution of secondary interactions by eventually generated δ electrons. The charge collected at the electrodes is approximately represented by the ratio of the carrier drift length, or charge collection distance, to the film thickness,

$$Q_c \approx Q_p \frac{d_c}{D} \quad . \quad (5.3)$$

Substituting Q_p with the expression in eq. 5.2 results in

$$Q_c \approx q_p d_c \quad . \quad (5.4)$$

The charge collection efficiency, which is defined as the ratio of measured charge to the total generated charge, is given by

$$cce \approx \frac{d_c}{D} \quad . \quad (5.5)$$

Eq. 5.4 tells that the charge collected at the electrodes is a function of the mean collection distance only. However, with thicker films more charge is generated, thus more charge is collected and the charge collection increases. Thus, the charge collection distance, together with the sample thickness, state the material quality.

In order to increase the signal size, the diamond film can be grown thicker. On the other hand, tracking detectors must be kept as thin as possible. The solution that complies with both requirements is to grow a rather thick diamond film and then remove, by lapping, material from the substrate side, where the collection distance is very low. Due to surface limits, the mean charge collection passes its maximum and decreases, if too much material is removed. It has been shown by theory and experiment [23] that there is an optimal remaining thickness for given detector parameters. The collection distance increase using this technique ranges up to 40% with present diamond samples. Fig. 5.1 shows the charge collection distances of two different diamond samples after several steps of lapping. The measured values agree with the theory well. For the application as a tracking detector is the target to achieve a thin detector with sufficient signal output.

Apart from the local collection distance depending on the depth as discussed above, the diamond film is considered to be laterally homogeneous. Measurements have shown

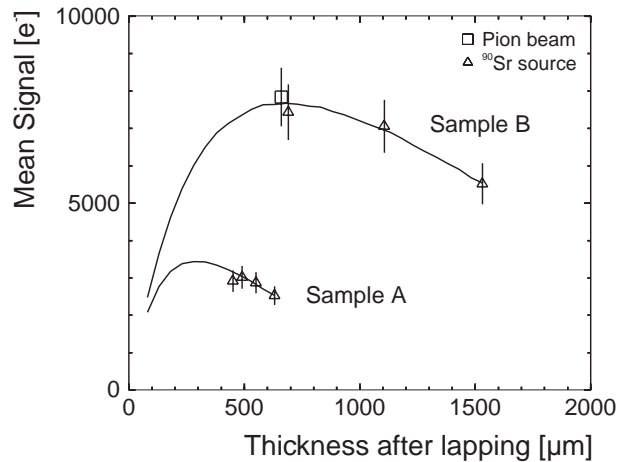


Figure 5.1: Charge collection distance vs. thickness remaining after lapping for two different diamond samples. The solid line shows the prediction from a calculation including border limits.

that this is not true with CVD diamond samples. Significant lateral variations of the collection distance have been encountered on the scale of a few ten micrometers. On some samples, clusters with higher or lower local d_c than the average have been observed in the sub-millimeter range, which may correspond to the grains. These effects are currently under investigation. Fig. 5.2 shows a preliminary distribution plot of the charge collection distance in $100 \times 100 \mu\text{m}^2$ bins. Each bin contains approximately 120 hit entries and the shade represents its mean collection distance. The white column to the right corresponds to a dead readout channel. The histogram at the bottom shows the distribution of the overall collected charge, which is not exactly Landau-shaped due to the inhomogeneity. It is intended to achieve smaller binning and higher statistics in the future.

Whenever a charge collection distance value is stated within this work, it is meant to be the average over a comparatively large volume of the diamond film. The radiation hardness studies in particular have been made on diamond samples with pad electrodes covering an area of 2.5 mm^2 and more.

Natural diamond has a charge collection distance of about $30 \mu\text{m}$. Starting in the early 1990s, the d_c of CVD diamond was far below this value. From that time, the collection distance was permanently improved by refining the manufacturer's growth process as shown in fig. 5.3. By the end of 1997, diamond detectors with a charge collection distance of up to $250 \mu\text{m}$ (corresponding to a mean signal of 9000 e) were available. Although those detectors were rather thick (almost 1 mm), a recent sample shows $d_c = 230 \mu\text{m}$ while it is only $432 \mu\text{m}$ thick, resulting in a charge collection efficiency of 53%.

5.1.2 Collection Distance vs. Electric Field

As in all solid state detectors, the charge collection speed depends on the strength of the electric drift field. This behavior originates in the carrier drift velocities, which are a function of the electric field, approximated in the linear region by

$$v = \mu E \quad . \quad (5.6)$$

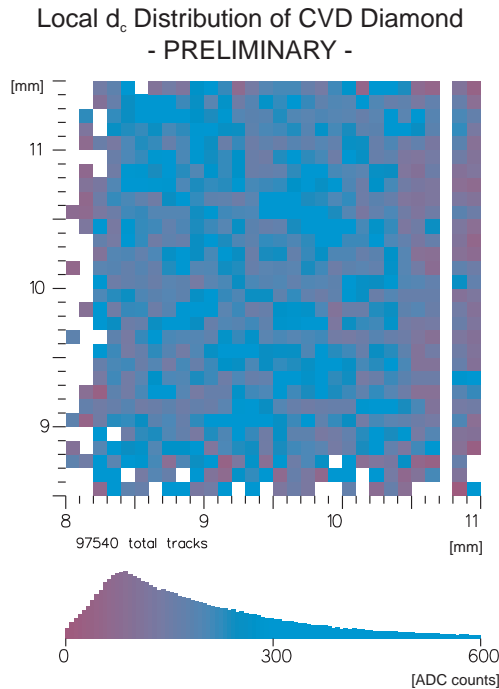


Figure 5.2: Spatial distribution of the local charge collection distance. The histogram at the bottom gives the distribution of the overall collected charge.

The velocities saturate with higher electric field. As the target is to achieve the highest possible charge collection efficiency, one aims to apply an electric field close to saturation. On the other hand, high voltages are difficult to handle and there is the danger of electric break-through. Thus, the usual field strength for CVD diamond characterization has become $1 \text{ V } \mu\text{m}^{-1}$, resulting in an applied voltage of several hundred Volts, depending on the sample thickness.

In fig. 5.4, the dependence of the charge collection distance on the applied electric field for a high-quality diamond is shown. Measurements with reverse polarity of the electric field show that there is no significant asymmetry, thus there is no sign of long-term polarization effects.

5.2 Si Detectors

Most solid state tracking detectors presently used are made of silicon, a material that is easily available from the semiconductor industry and well understood. However, silicon for detector application must be of higher quality and purity than the material for semiconducting devices.

The intrinsic carrier density of silicon is too high to operate a silicon detector as-is. This should be illustrated by a comparison [25] for a commonly used detector thickness of $300 \mu\text{m}$ and an area of 1 cm^2 . The number of intrinsic carrier pairs inside the bulk volume is 4.35×10^8 , while one MIP traversing the detector generates a mean signal of only 32400

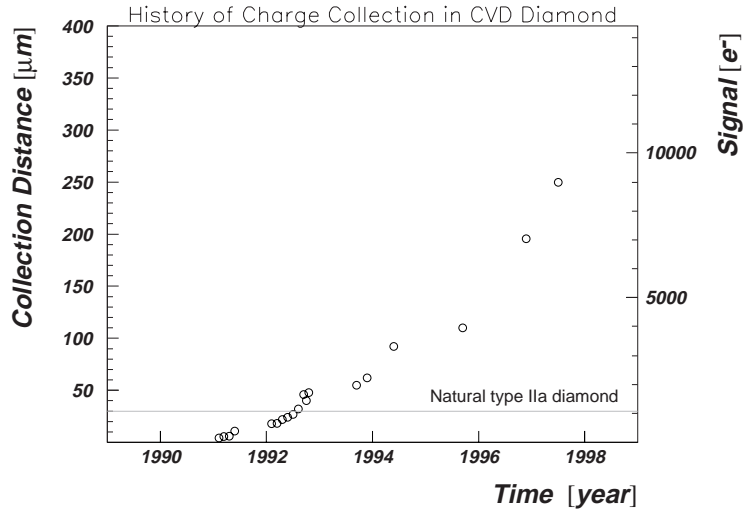


Figure 5.3: The history of the charge collection distance of CVD diamond.

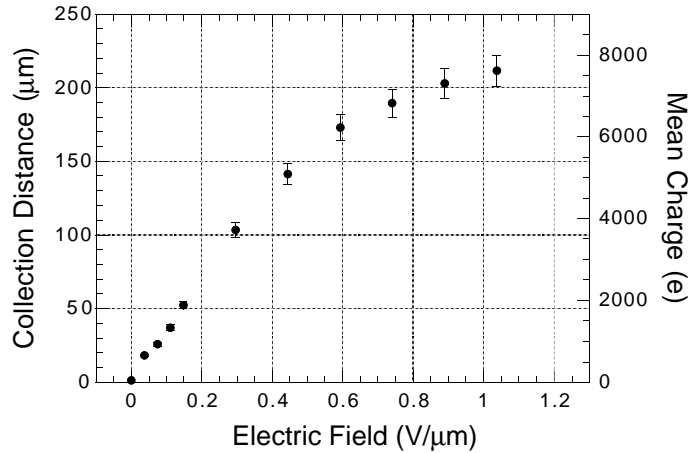


Figure 5.4: The collection distance vs. the electric field.

pairs.

In order to remove the intrinsic charge from the bulk, a pn-junction is introduced. Usually starting with a weakly doped n-type silicon wafer, a thin layer on one side is heavily doped with boron acceptors, and a thin layer on the opposite side with arsenic donors, resulting in a p^+n^- -diode. Alternatively, the bulk material can be of p-type, which makes no principal difference. Finally, the surfaces are metallized to form Ohmic contacts. When the pn-junction is reverse-biased, all free carriers are drained from the bulk, and the detector is sensitive to ionizing radiation. Fig. 5.5 shows such a silicon detector with the applied bias voltage, which is above the depletion voltage¹, and the resulting electric field. The implant layers are much thinner in reality, thus a the electric

¹The depletion voltage is the minimum bias voltage required to establish a space charge zone across the whole bulk

field is approximately constant throughout the bulk. Principally, the silicon detector is a wide-area diode.

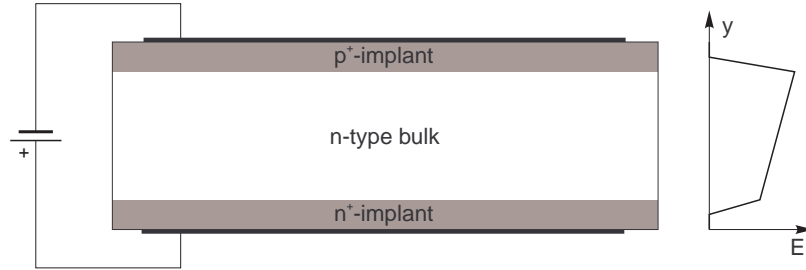


Figure 5.5: Schematic cross-section of a silicon detector with implant thicknesses not to scale. The electric field results from a bias voltage above the depletion voltage.

Silicon detectors are made of very pure material, minimizing the number of charge traps and recombination centers. Nearly all charges excited in the bulk reach the electrodes, implying a charge collection efficiency of (almost) 100%. According to the charge mobilities, the charge collection after a particle traversed the bulk takes a few nanoseconds.

5.3 Ge Detectors

Germanium was the first technically used semiconductor material. As the specific energy loss dE/dx is quite high in germanium compared to silicon, it better suits for calorimetry than for tracking purposes. For instance, lithium-drifted germanium detectors [26] with an active crystal volume of several cm^3 are used in nuclear spectroscopy. These detectors achieve an excellent energy resolution, however, they must be permanently cooled to liquid nitrogen temperature ($T = 77\text{K}$). The low temperature not only conserves the arrangement of the lithium atoms inside the crystal, but also reduces the intrinsic carrier density dramatically. Only this fact permits the functioning of the device.

Later, it became possible to produce extremely pure germanium material, which is more convenient to use. Still low temperature operation is essential, but an interruption of the cooling is no longer disastrous.

5.4 GaAs Detectors

Gallium-arsenide is a III-V-type semiconductor. The semiconducting junction is introduced through a Schottky contact on the bulk material. Unlike silicon, the electric field does not extend throughout the bulk [9], in fact, there is a passive layer with zero field and the field in the active layer is decreasing from a maximum at the Schottky contact to zero. Depending on the sample purity, there is a certain number of inter-band gap traps. Thus the charge collection efficiency of the best samples is presently at the order of 50% to 80%.

Chapter 6

Characterization

An important issue for judging the quality of a detector is the measurement of its charge collection distance, therefore called characterization. In a laboratory environment, the detector under test is exposed to a source and the pulse height spectrum is recorded. Principally, it is the same measurement that is also made in test beams or detectors in experiments, although in the laboratory more emphasis is laid upon precise measurements, well-defined parameters, reproducibility and a clean analysis.

6.1 Characterization Setup

The main elements of a characterization setup are the detector itself, a particle source and a front-end amplifier as well as trigger and readout electronics. A few institutes participating in the RD42 collaboration have built such characterization stations. As an example, the setup at the HEPHY is shown schematically in fig. 6.1. When a particle from

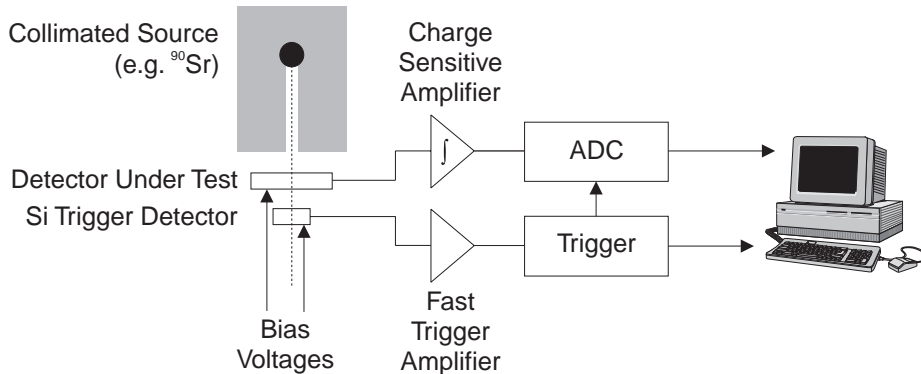


Figure 6.1: Schematics of the characterization station.

the source traverses the detector under test and the trigger detector, a readout cycle is initiated, the amplifier output is converted to digital numbers and stored in the computer.

Apart from the detector itself, the involved parts will be discussed in the following sections.

6.1.1 Particle Source

Penetrating particles are necessary for tracking detector measurements, either coming from an accelerator, a radioactive source or from cosmic radiation. The characterization of tracking detectors usually refers to minimum ionizing particles (MIPs), which transfer the least amount of energy possible (see section 4.1).

The muons of cosmic radiation are not suitable for detector tests, since the sensitive area is usually very small ($< 1 \text{ cm}^2$), which results in a very low cosmic rate. Exact reference measurements require a well defined particle beam, which is only available from high energy accelerators such as the SPS (Super Proton Synchrotron) at CERN.

However, for practical reasons, it is much easier to use a radioactive source such as ^{90}Sr , which delivers only beta electrons. In the setup shown in fig. 6.1, the detector under test is located between the source and the trigger detector. Electrons with low energies thus stop in the test detector without triggering. This method requires a source with rather low activity, otherwise such a stopping electron and a subsequent (or previous) penetrating electron could overlap within the time constant of the amplifier, leading to false signal pulse heights and pile-up effects.

Assuming a $500 \mu\text{m}$ thick diamond detector, electrons with a kinetic energy below roughly 0.5 MeV are absorbed. The penetrating particles are a good approximation to MIPs; in $500 \mu\text{m}$ thick diamond they deposit 108% of the MIP energy [8]. Strontium decays in β^- mode to ^{90}Y , emitting electrons with a maximum energy of 0.55 MeV [13, 27], most of which do not penetrate the detector under test. The half-life of this first decay is 28.8 years. The ^{90}Y isotope again decays in the β^- mode with a half-life of 64.1 hours to the stable ^{90}Zr isotope; the maximum energy of the electrons is then 2.28 MeV . The practical result of this decay chain is in fact a ^{90}Y decay with a half-life of 28.8 years rather than 64.1 hours [28].

The advantages of ^{90}Sr compared to other isotopes are the lack of γ decays, the relatively narrow energy spread and the long half-life, which results in almost constant activity over years. For most applications it is necessary to collimate the source, as the electrons are emitted in all directions. Furthermore, the collimator has the task of protecting the person handling the source.

Due to the low energy, the range of such β electrons in solid matter is only a few millimeters, depending on the kind and amount of material in the particle track. For measurements where further penetration of the particles is essential, a high energy particle beam from an accelerator is essential. This may be the case when particle tracks are monitored with a telescope (see section 8.2) or the response of the detector to specified particles and energies is under investigation. However, these studies are usually described as test beam measurements and not as characterization.

6.1.2 Detector Amplifiers

After a particle has traversed the detector, a certain charge is induced in the electrodes. In the case of MIPs, this charge is of the order of several thousand electrons (and holes), which have to be amplified to a reasonable voltage (or current) level.

The preamplifier, which is physically connected to the detector, is the first stage of the amplifier chain. There are two principal configurations [10, 29], the feedback preamplifier (or charge-sensitive amplifier), which is slow but accurate, and the grounded base amplifier, which is fast but contributes more noise.

The performance of the preamplifier is primarily determined by the noise figure, which is usually stated in terms of equivalent noise charge (*ENC*). As the electronic noise is approximately Gaussian distributed, the *ENC* states the *RMS* value of a noise charge source at the input of the (fictive) noise-free amplifier. The *ENC* depends on the electronic parameters of the input stage and approximately linearly increases with load (detector) capacitance.

Within the characterization station, both types of preamplifiers are used. A low-noise, slow charge-sensitive amplifier is connected to the detector under test, while a fast grounded base amplifier, connected to a silicon diode, is used as a trigger detector.

6.1.2.1 Charge-Sensitive Amplifier

The feedback preamplifier basically relies on the current integrating capability of a capacitor, given by

$$CV = \int Idt = Q \quad . \quad (6.1)$$

There are various realisations of charge-sensitive amplifiers in both discrete and integrated circuits. It is easily seen that the latter have a much better noise figure. As an example, I want to give some details of the VA2 chip, which was used for the characterization station at the HEPHY. The VA2 chip, produced by the IDE AS company [30], is a lower noise redesign of the original Viking chip [31, 32] for silicon strip detector readout. It has 128 equal input channels, one of which is connected to the detector under test.

The schematics of the input stage of one channel is shown in fig. 6.2, composed of the preamplifier, which actually converts charge to voltage, and the shaper. The preamplifier

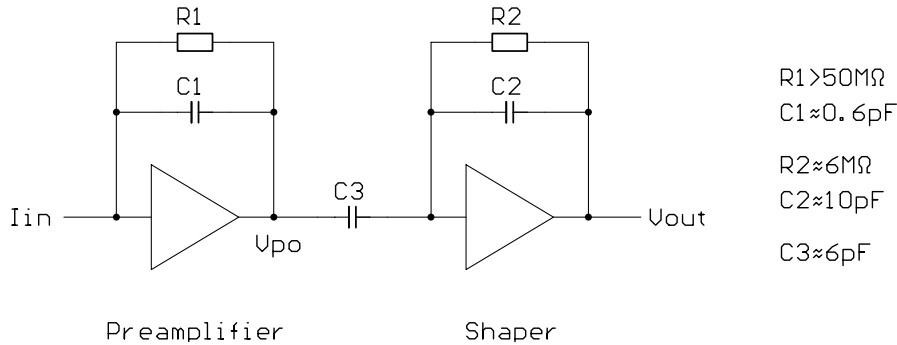


Figure 6.2: Schematics of one VA2 input stage, consisting of preamplifier and shaper.

integrates the input current, while resistor R_1 slowly discharges the integrating capacitor C_1 to avoid pile-up effects. The output of the preamplifier is connected to a CR-RC shaper, which filters the preamplifier output in order to minimize the noise. Both preamplifier and shaper make use of operational transconductance amplifiers (OTAs). The resistors

and amplifier bias currents are adjustable to optimize the output signal with respect to the detector parameters.

When a particle traverses the detector, a current pulse is injected into the detector with a duration of approximately one (diamond) or a few (silicon) nanoseconds. With respect to the system's time constants, this input current can be simplified in both cases without loss of accuracy to a Dirac delta pulse. The preamplifier integrates this current pulse, resulting in a step pulse, while the discharging effect of resistor R_1 can be neglected comparing the time constants. This step pulse is now shaped by the CR-RC stage, which has the (Laplace domain) transfer function

$$H(s) = \frac{V_{\text{out}}}{V_{\text{po}}} = A \frac{sT_p}{(1 + sT_p)^2} \quad (6.2)$$

T_p is the peaking time of the output signal, i.e., the time from the charge injection to the maximum of the output voltage and thus the point to sample. According to the bias settings, it can be adjusted in the range of $0.5 \dots 3 \mu\text{s}$. The internal logic of the VA2 provides a sample/hold circuit and an output multiplexer, shifting out all 128 sampled values in an analog queue, which are digitized externally. Basically two reasons do not allow an on-chip ADC: the effects on the system noise and the additional power consumption (note that several thousands of such chips are utilized in a vertex detector in a comparatively compact volume at an operating temperature of slightly below 0°C).

Due to the long integration time, the noise figure of this amplifier is excellent. For the original Viking chip a value of approximately $ENC \approx 135 e + 12.3 e \text{ pF}^{-1}$, slightly depending on the peaking time, is stated, while the noise of the VA2 redesign, which is optimized for lower load capacitance, could be reduced to $ENC \approx 82 e + 14 e \text{ pF}^{-1}$.

6.1.2.2 Grounded Base Amplifier

A second particle-sensitive detector is necessary in order to trigger a readout cycle of the amplifier connected to the detector under test. Often these are one or more scintillators connected to photomultiplier tubes. In our setup we decided to use a standard silicon detector connected to a very fast, discrete amplifier described below. The major advantages of this trigger compared to a scintillator-photomultiplier combination are its compact size and the lack of high voltage, which would be essential for a photomultiplier. Apart from that, as both the trigger and the test detector are solid state detectors, they sense the same set of particles, i.e., only charged particles. Scintillators, however, are also sensitive to neutral particles.

The trigger amplifier utilized in the Vienna characterization station is a very fast, non-integrating grounded base amplifier [33]. This circuit, shown in fig. 6.3, directly converts the input current to an output voltage, allowing to monitor the charge collection duration in various detector types.

The preamplifier makes use of low cost HF transistors (2SC4995), which have a transit frequency of $f_t = 11 \text{ GHz}$, a DC gain of $h_{fe} = 120$ and a noise figure of $a_F = 1.1 \text{ dB}$ at $f = 900 \text{ MHz}$. A monolithic amplifier (INA-02186) giving a gain of 30 dB and a pass-band flat to 1 GHz, is implemented after the preamplifier, capable of driving a 50Ω line. In

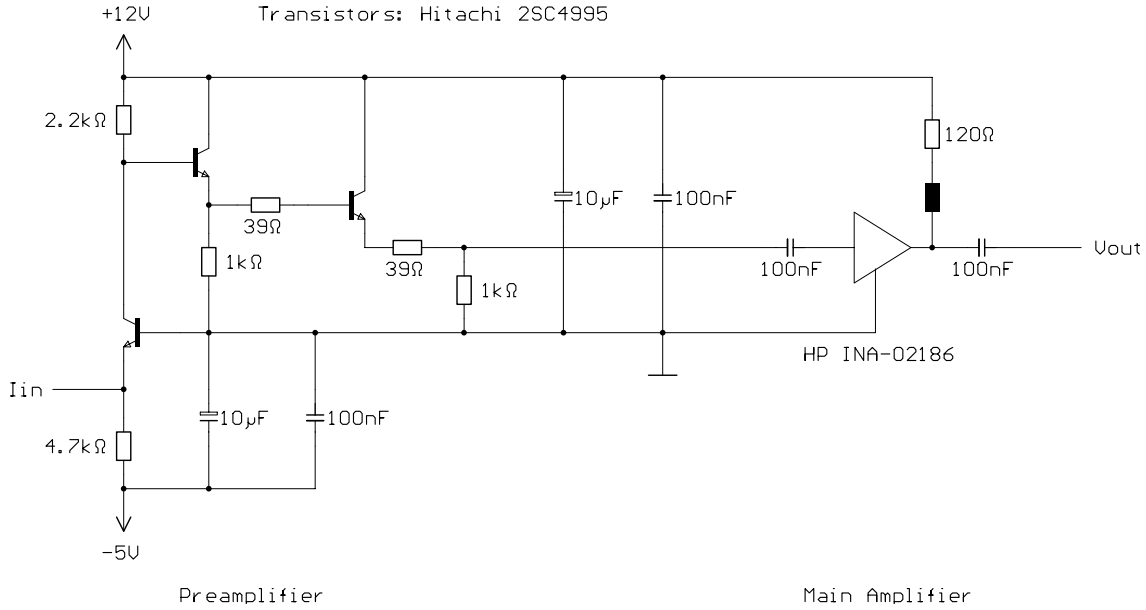


Figure 6.3: Schematics of the grounded base trigger amplifier.

order to cut off low frequency ($1/f$) noise, a miniature transformer was utilized in the prototype tests discussed in [33]. In our setup we used a simple RC combination of low and high pass, providing similar signal processing.

The risetime of the amplifier is specified to be < 600 ps, while the noise is stated to be $ENC \approx 1000 e + 60 e pF^{-1}$. Compared to the integrating charge-sensitive amplifier discussed above, basically accuracy is sacrificed for speed.

6.1.3 Readout Electronics

The front-end electronic is very sensitive against any kind of electric influence. Therefore, a central ground point is essential, together with the shielding of the complete setup. In the Vienna characterization station, the front-end has been packed into a copper-shielded box, which is kept closed during measurement. This is also necessary as the detectors and the VA2 chip are sensitive to light. Fig. 6.4 shows a photograph of the box. During measurements, the lid is closed and the collimator with the source mounted onto it. Fig. 6.5 shows the detailed schematics of the Vienna characterization station. The diamond detector is AC coupled to the VA2 to allow different potentials. As the VA2 chip output stage obviously is not very powerful, a repeater card (designed by A. Rudge and the Ohio State University) is foreseen, which buffers both incoming and outgoing VA2 signals.

For calibration purposes, a well defined step pulse is attenuated and sent to the VA2 input over a small capacitance, injecting a charge of

$$Q = C\Delta V \quad . \quad (6.3)$$

There are two separated voltage dividers in the attenuator, because inevitable stray ca-

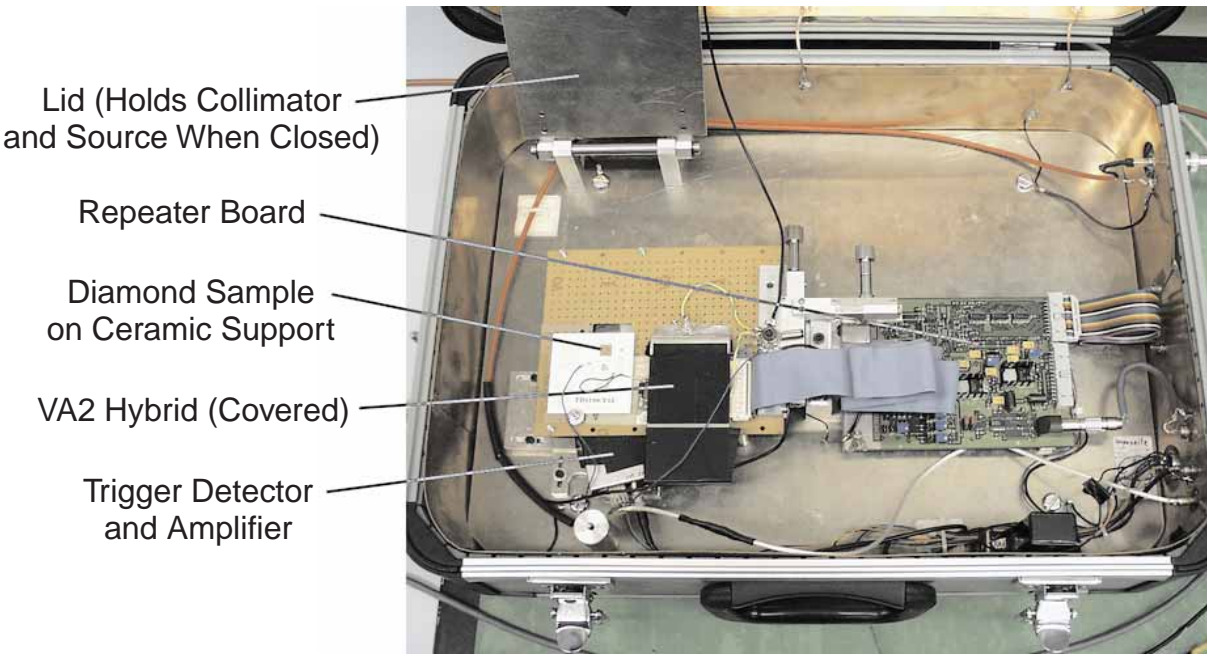


Figure 6.4: The Vienna characterization station.

capacitance results in capacitive rather than galvanic coupling if the division ratio becomes too high.

The data acquisition and control in the Vienna setup is done using CAMAC modules and an Apple Macintosh IIx computer. The CAMAC crate is equipped with a non-standard Bergoz MAC-CC controller, while the Mac utilizes a Micron card to establish the connection.

The detector bias voltage is provided by a commercial CAMAC HV module (Struck CHQ203A). A module built by the Ohio State University (OSU M663A) handles the VA2 triggering and readout, while a home-made CAMAC module is responsible for general control, trigger decision and calibration pulse generation.

6.1.4 Data Acquisition Software

On the Macintosh computer, a data acquisition program called Diamond Station has been written in the LabView 3 environment by H. Pernegger and myself. This software controls the CAMAC modules and reads out the VA2 analog data when a trigger condition occurs. The data is filled into a histogram, collecting the signal pulse height spectrum, which is displayed online and written to disk for offline analysis. The program is also capable of automatically recording a measurement series with one detector, sweeping the bias voltage and taking pedestals before and after. In previous versions, a common mode correction (CMC) algorithm was included, which turned out to have no significant effect except slowing down the whole measurement. Fig. 6.6 shows a screenshot of the Diamond Station program.

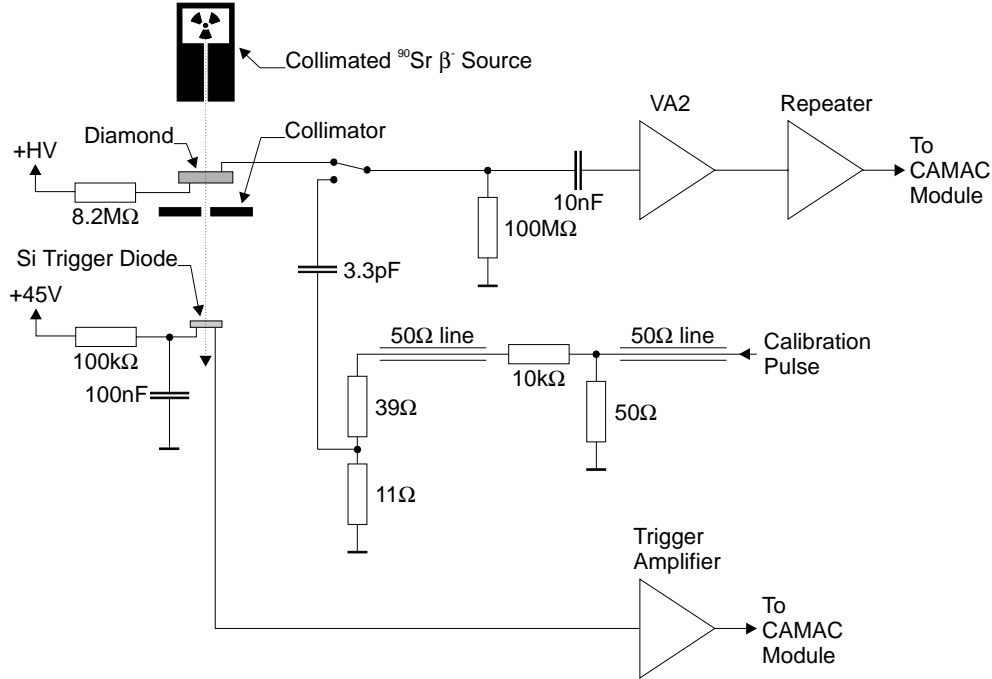


Figure 6.5: Schematics of the Vienna characterization station.

6.2 Calibration and Noise Measurements

With a pedestal measurement, the overall noise performance of the characterization setup can be determined. However, this is only given in ADC counts, as long as there is no absolute calibration, which can be done through the injection of a known step pulse into the VA2 input as described above.

To obtain an accurate calibration, it is essential to know the involved parameters, in particular the exact capacitance value (C) and the voltage step size at the capacitor. The capacitor has been measured with a Hewlett Packard 4285A precision LCR meter, while the small voltage step cannot be measured directly with required precision. Thus, the attenuation of the voltage dividers (r) has been measured with DC voltages much higher than used in the calibration. The step pulse output of the CAMAC module can be switched alternatively to both DC levels to precisely measure the voltage difference before attenuation (ΔV). The number of electrons injected into the VA2 is given by

$$N = \frac{Q}{e} = \frac{C\Delta V}{re} . \quad (6.4)$$

The rise time of the step pulse is indifferent, as long as it is substantially shorter than the integration time of the VA2, which is also the minimum length of the pulse.

Fig. 6.7 shows a measurement of both pedestal and calibration peaks in the pulse height spectrum, fitted with Gaussian distributions. In this case, the parameters were $C = 3.37$ pF, $\Delta V = 227.6$ mV (terminated) and $r = 1022$, yielding an injected charge of 4691 e. From the histogram fit parameters, a pedestal *RMS* of 3.192 ADC counts and a peak location difference of 70.9 ADC counts are obtained.

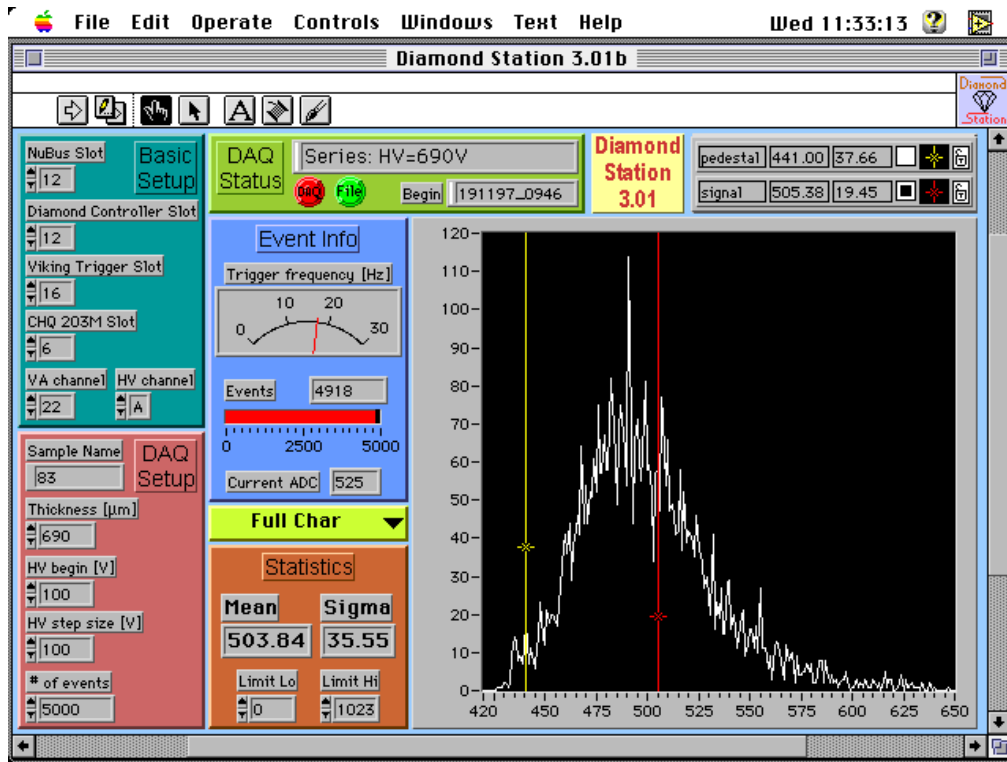


Figure 6.6: Screenshot of the Diamond Station data acquisition software.

Finally, the calibration constant is $C_{\text{cal}} = 66.2 \text{ eADC}^{-1}$, and the noise figure is $\sigma = 211 \text{ e}$. With a diamond detector connected, the latter slightly increases due to additional wiring to the order of $\sigma = 270 \text{ e}$. VA2 channels which are not connected show an *ENC* of approximately $\sigma = 93 \text{ e}$. This figure comes close to the value stated by the VA2 manufacturer. The reason for the excess noise of the input channel is the external wiring. The placement and values of the elements in this circuit are critical and have been optimized empirically, but they still add thermal and other noise and stray capacitance.

The pedestal mean value is subjected to a mid-term drift due to temperature variations, while the calibration constant (or, gain) turned out to be quite stable. Therefore, the pedestal has been taken before and after each measurement series, while the calibration was done occasionally.

6.3 Fit Model

With a homogeneous detector material, a “perfect” Landau distributed pulse height spectrum is expected. In practice, a small fraction of particles, due to misalignment and scattering, traverse the trigger, but not the test detector, thus adding a small pedestal contribution to the spectrum. The signal and pedestal parts are well separated with silicon detectors. However, with diamond samples, especially those with low collection distance, the two contributions cannot easily be distinguished. Fig. 6.8 shows two examples of pulse

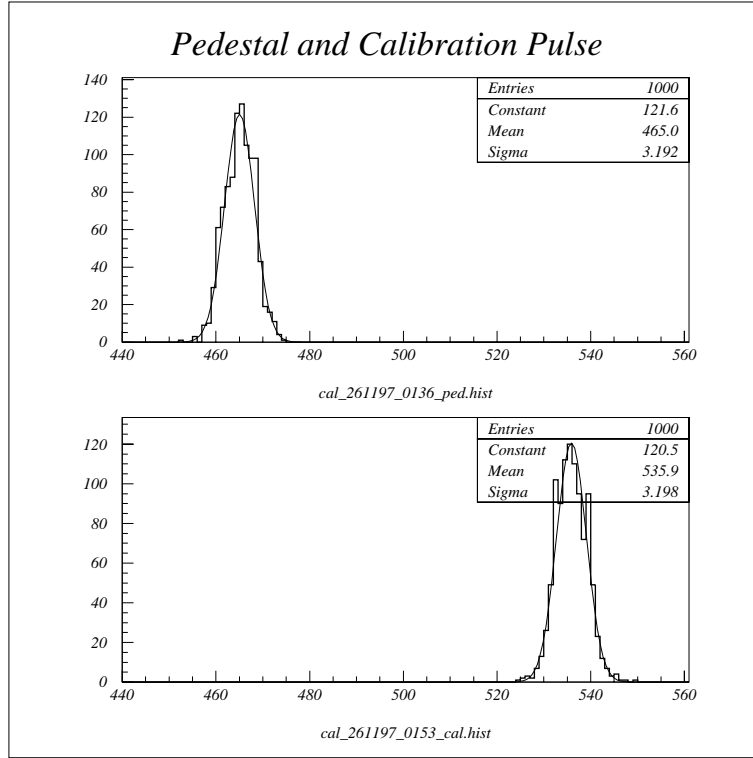


Figure 6.7: Pedestal and calibration measured histograms with Gaussian fits applied.

height histograms. The left figure corresponds to a sample with low collection distance, where pedestal and signal parts cannot be separated. On the contrary, the right histogram is of a high quality sample, where separation is easier.

Neglecting any noise contributions, we would expect a Dirac delta needle at the pedestal position plus a Landau distribution. Taking the electronic noise into account, we have to convolute the spectrum with a Gaussian distribution, having a width σ as observed from the pedestal contribution, resulting in

$$\mathcal{H}_F = [\delta(\text{pedestal}) + \mathcal{L}(\text{signal})] * \mathcal{G}(\sigma) = \mathcal{G}(\text{pedestal}, \sigma) + \mathcal{L}(\text{signal}) * \mathcal{G}(\sigma) \quad . \quad (6.5)$$

This model is illustrated by fig. 6.9.

However, as CVD diamond has a columnar structure in the growth direction and also considerable lateral inhomogeneities (see section 5.1.1), the spectrum does not exactly follow this shape. In fact, a superposition of various Landau distributions occurs, yielding a broader shape. Therefore, we convolute the signal related to the Landau part in eq. 6.5 with a Gaussian distribution with a σ greater than that of the pedestal.

Thus, the final fit model is

$$\mathcal{H}_F = \underbrace{\mathcal{G}(\text{pedestal}, \sigma)}_{\text{pedestal}} + \underbrace{\mathcal{L}(\text{signal}) * \mathcal{G}(\sigma_{\mathcal{L}})}_{\text{signal}} \quad \text{with } \sigma_{\mathcal{L}} > \sigma \quad . \quad (6.6)$$

The solid lines in fig. 6.8 show the fit results with this function. When the pedestal mean and σ , which are known from pedestal runs, are kept constant and reasonable initial

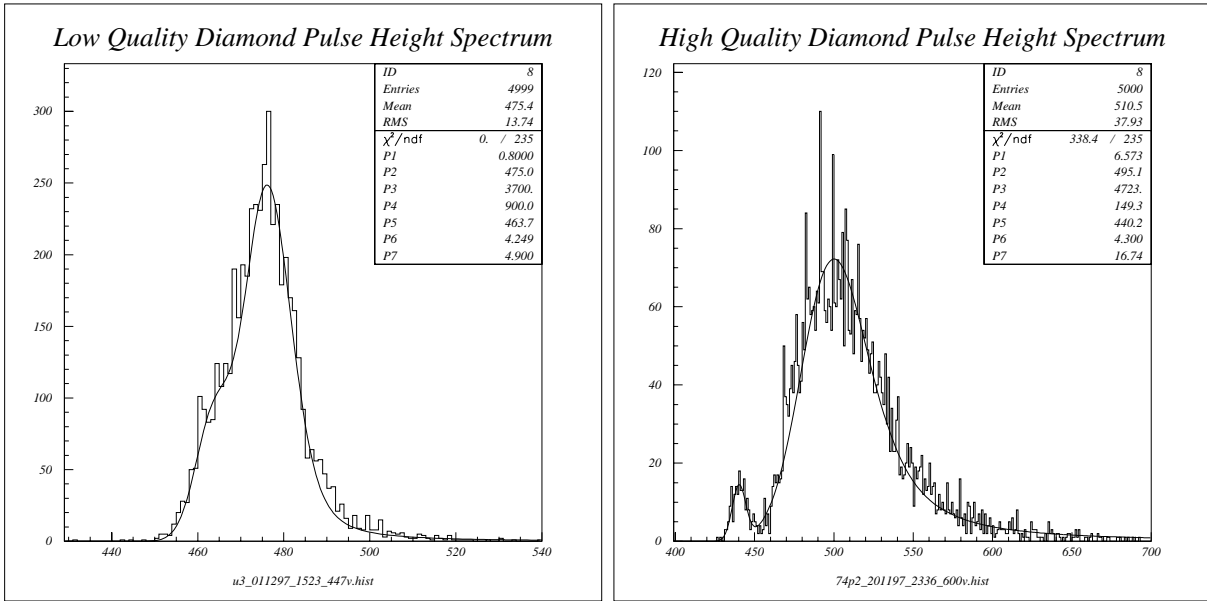


Figure 6.8: Typical diamond pulse height spectra. The histogram to the right shows a high d_c sample, where pedestal and signal are clearly separated, which is not the case in the left histogram of a low d_c diamond. The solid line shows the applied fit function (see text below).

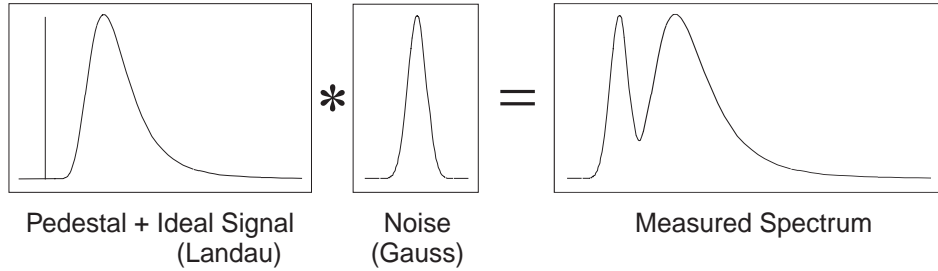


Figure 6.9: A model for fitting histograms.

values are given, the fit also works with low quality diamonds, as shown in the left plot of fig. 6.8.

After obtaining the fit parameters, the question of the mean signal remains. As discussed in section 4.2, the ideal Landau distribution does not have a mean value. The Landau fit, however, provides a weight, which corresponds to the area below the curve. With the mean value and the area below the Gaussian pedestal fit curve, which are also resulting from the fit, the pedestal contribution can be subtracted from the mean value of the measured histogram, resulting in a signal mean. Finally, we obtain the charge collection distance by multiplying the difference between signal and pedestal means with the calibration constant (C_{cal}),

$$d_c = C_{\text{cal}} \left(\frac{\text{area}(\text{signal}) + \text{area}(\text{pedestal})}{\text{area}(\text{signal})} \right) (\text{mean}(\mathcal{H}) - \text{mean}(\text{pedestal})) \quad . \quad (6.7)$$

For diamonds with reasonable pedestal separation (right histogram in fig. 6.8), it is

much easier to calculate the charge collection distance by simply cutting out or subtracting the pedestal contribution. This approach has been cross-checked with the fit method, yielding similar results.

Usually, the pedestal contribution in the pulse height histograms makes up a few percent of all events and thus is negligible. Yet, in some cases, the pedestal may even dominate the spectrum. If the metallization dot on the diamond sample is smaller than the collimator hole, a considerable amount of particles cross the diamond without inducing a proper signal. Due to the fringe field, the signal is non-zero, but significantly smaller than the true signal. The result is a “merging” of pedestal and signal distributions. Another reason for increased pedestal contribution is given when measuring in between irradiation periods, where the diamond itself, the metallization and the ceramic support are activated. These parts emit particles that reach the trigger but do not traverse the diamond, generating “false triggers”. Various isotopes with different lifetimes are produced; one major product, coming from aluminum in the Al_2O_3 ceramic support, is ^{24}Na with a half-life of 15 hours. Generally, it takes a couple of weeks until the activity of all isotopes drops to a negligible rate.

Chapter 7

Radiation Hardness

7.1 Radiation Defects

The properties of diamond may be affected by impurities in the lattice. Especially, the charge collection distance strongly depends on the presence of inhomogeneities.

Atoms that do not fit into the diamond lattice or lattice positions that are not occupied are called defects in general. In the virgin state, CVD polycrystalline diamond has a certain number of defects, depending on the growth parameters. In particular, there are considerable nitrogen impurities. Additionally, the grain boundaries are suspected to provide a significant number of charge traps and recombination centers. The defects introduce energy levels inside the band gap. As the carrier transition between valence and conduction bands becomes more probable with the introduction of intermediate levels, the intrinsic carrier density increases, resulting in a higher leakage current. However, as diamond has a very large band gap, and the impurities in detector material are below the ppm range, the bulk current remains negligible in practice. In fact, no significant effect has been observed on the leakage current before and after the irradiation experiments.

Additional defects are introduced with irradiation [6]. Depending on the incident particle type and momentum, various defects may occur by atom displacement. With low momentum particles, only simple defects are probable. These are vacancies, where a lattice position is unoccupied and interstitials, where an atom is posed in between the lattice. Due to the conservation of matter, these two always occur together, called Frenkel defects. Heavy particles, especially ions, usually have a very short range in the order of micrometers. They are stopped in the diamond films, transferring their whole energy and additionally placing themselves in the diamond lattice. For this reason, the damage induced by ions, is by orders of magnitude higher than that of traversing particles.

All of these defects affect the charge collection efficiency by the creation of trapping and recombination centers, which decrease the carrier lifetime and thus the drift distance.

Considering the tightly bound, compact lattice, diamond has a reputation of being quite insensitive to radiation. However, as theoretical prediction is difficult, experiments have been carried out to observe the damage introduced by various kinds of particles.

7.2 Pumping Effect

A diamond detector that has never been irradiated before is in a virgin state, called “unpumped”. With moderate irradiation fluence, the signal output, or charge collection distance, increases significantly. The cause for this unique behavior are defects of the material. There are non-diamond atoms in the bulk, generating energy levels inside the band gap, which act as charge traps. With irradiation, these traps are filled and made inactive, thus they do no longer absorb electrons or holes. When all such traps are passivated, the diamond is called “pumped” and this state is conserved until the diamond is exposed to UV light. By UV absorption, the trapped charges are released again, resetting the diamond to its original, or unpumped state. Present understanding is that this procedure is fully reversible and there is no limitation in the number of pumping/unpumping cycles.

The pumping transition occurs with all types of particles and needs a radiation fluence of approximately 10^{10} particles cm^{-2} . With this fluence, the collection distance increases by 30 to 100%, depending on the sample. Fig. 7.1 shows the pumping effect by exposure to a ^{90}Sr source. Recent measurements show that the fluence needed for complete pumping increases after intense irradiation, indicating an increased number of traps in the diamond bulk, as expected. A linear relationship between pumping fluence and irradiation fluence has been observed.

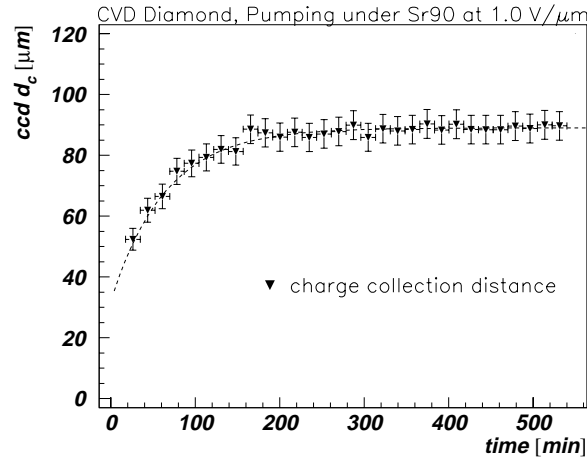


Figure 7.1: The pumping effect during exposure of a diamond sample to a ^{90}Sr source.

In future experiments such as the LHC, diamond detectors will reach the pumped state within several hours, depending on the luminosity and the distance from the vertex. As this will be the working condition, all charge collection distance values are given in the pumped state unless noted otherwise.

7.3 Irradiation

Several diamond detectors were exposed to high intensity photon, electron, pion, proton, neutron and α particle beams. During all irradiation runs, the detectors were biased, resulting in an electric field strength of 0.2 to 1 V μm^{-1} , to obtain similar conditions as in future applications.

As a representative example, the pion irradiation will be discussed in more detail.

7.3.1 Pion Irradiation

Four pion irradiation experiments have been carried out at the Paul Scherrer Institute (PSI), Villigen, CH, in the past years [34].

All experiments were performed with 300 MeV c^{-1} π^+ . This choice was based on the Δ resonance peak for the π^+p interaction, as shown in the top half of fig. 7.2 [13]. The bottom plot shows that there is no such significant peak for π^- . Due to the high cross section, the chosen particles are expected to induce more radiation damage than those with other momenta.

Fig. 7.3 shows the beam setup. The diamond samples had an average thickness of 650 μm and were biased with 300 V ($E \approx 0.5 \text{ V } \mu\text{m}^{-1}$) throughout the irradiation. A carbon shield with a thickness of 3 cm reduced the proton contamination of the beam to the order below 1%. The diamonds were placed in the beam focus, which had a FWHM (full width at half maximum) of a few centimeters. Thus the irradiation on the samples was approximately homogeneous with a pion flux about $2 \times 10^9 \text{ cm}^{-2} \text{ s}^{-1}$.

On the back of each diamond sample an aluminum foil of extreme purity (99.999) was attached for dosimetry. ^{27}Al atoms are converted by pions to ^{24}Na with a half-life of 15 hours. This determined the length of each irradiation period, usually around 12 hours. After each period, the aluminum foils were put into a spectrometer to measure the amount of ^{24}Na produced. With irradiation and cooling times and the foil mass given, the received fluence can be calculated. The beam current was included in these calculations to take periods with no beam into account. The ionization chamber at the end of the beam pipe was used to cross-check the dosimetry results. The overall error of the dosimetry is estimated to be 15%.

During the irradiation, the beam induced current of each diamond sample was measured individually with a Keithley 237 source measure unit. The irradiation was performed without a cooling device, thus the sample temperature was about 25° C throughout the irradiation.

Individual samples were taken out of the beam in each irradiation period, rested for several hours and then were measured in the characterization station before re-insertion into the beam. The resting was necessary to reduce the radioactivity of the sample and the ceramic support. As mentioned in section 6.3, the pedestal contribution in the measured pulseheight spectrum increases with detector activity due to false triggers.

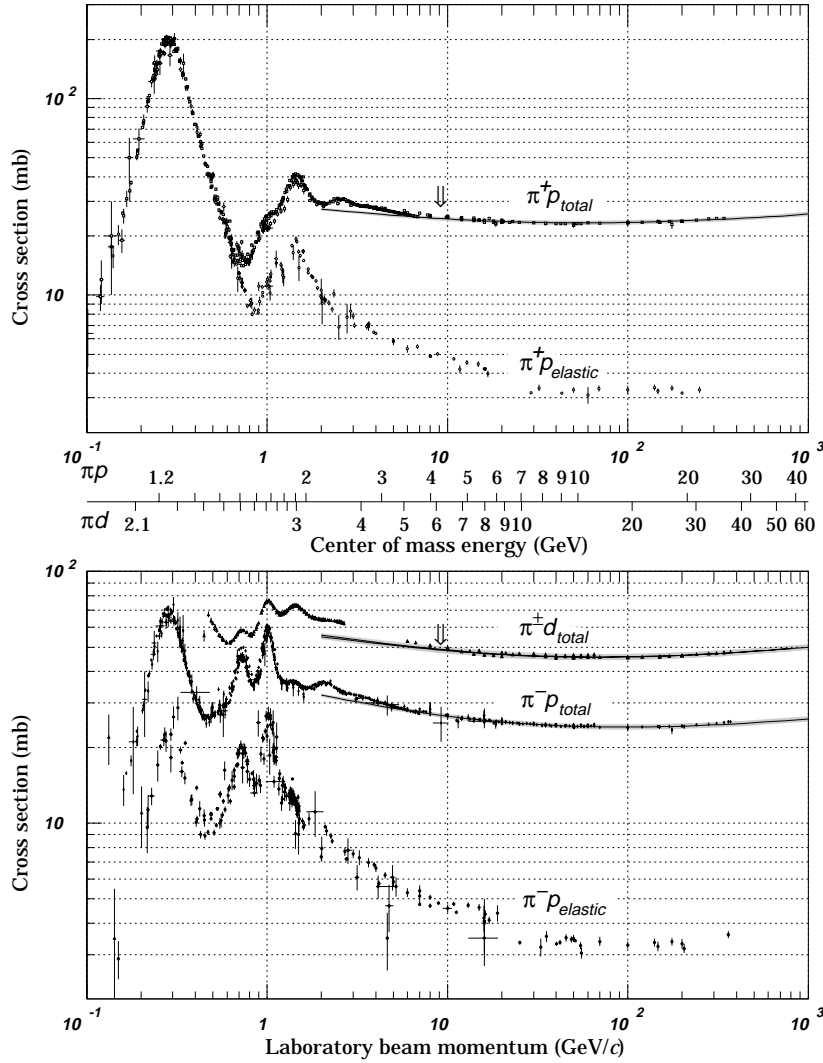


Figure 7.2: Nuclear interaction cross section plots for pions and protons.

7.3.1.1 Collection Distance

In fig. 7.4, the charge collection distance values in the pumped state are shown vs. pion fluence for various samples. The letter in the sample name indicates the wafer, from which the samples were cut. Apart from E1, always two corresponding samples from a wafer were irradiated, which behave similar.

It turned out that the higher the collection distance in the virgin state is, the faster it drops with irradiation. This behavior could be explained by the linear model. The vertical trap density in the detector before irradiation is higher at the substrate side than on the growth side, as discussed in section 5.1.1. Thus the local charge collection distance is low on the substrate side and high at the growth side. Intense irradiation is expected to introduce additional traps, equally distributed along the beam track. The sum trap density now increases significantly on the growth side, shrinking the local charge

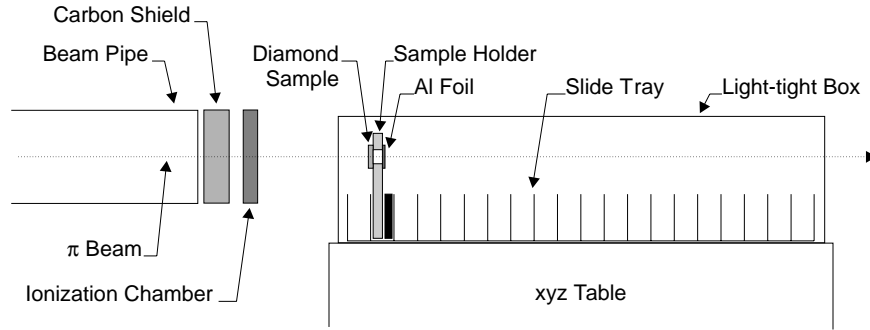


Figure 7.3: The irradiation setup.

collection distance, while there is only a negligible relative trap density increase at the substrate side. In other words, regions with a high charge collection distance are more susceptible to radiation damage than those with low d_c , which are relatively indifferent. Similar behaviour applies to the global (mean) charge collection distance, as observed in the experiment.

The measurements show that the signal decrease of the initially highest charge collection distance samples is about 40% after $10^{15} \pi \text{ cm}^{-2}$. This corresponds to the estimated fluence at the LHC at a radius of 7 cm from the vertex within 10 years of operation.

However, the irradiation damage is less severe than expected from the collection distance decrease, as the collection distance is calculated from the mean signal. When comparing the signal pulse height spectra in the pumped state before and after irradiation (fig. 7.5), it is visible that the radiation does not simply scale the whole distribution, but has more effect on initially higher signals, while there is almost no effect on very low signals. The Landau tail suffers from irradiation, the most probable value of the distribution is less affected and the rising edge almost stays the same. This agrees with the linear model damage discussed above, when we consider the inhomogeneity of CVD diamond. Regions with higher local collection distance are more affected by radiation than others, causing the strong effect on the Landau tail.

7.3.1.2 Beam Induced Charge

The ionisation process of $300 \text{ MeV } c^{-1}$ pions crossing the diamond is very similar to that of the electrons from the ^{90}Sr source, because pions with this momentum deposit approximately 110% of the MIP energy in diamond of $650 \mu\text{m}$ thickness [17]. The basic difference between the two types of irradiation is the flux, or intensity. While each single electron is observed during the characterization, there is a high pion flux during irradiation, which allows to measure a DC current, or average Q/t , respectively.

During beam-off periods, the current in the samples is essentially zero. When beginning the irradiation with a virgin sample, the beam induced current increases in the first couple of seconds due to the pumping effect. However, as the flux was not constant throughout the irradiation, it is more convenient for further analysis to look at the beam induced charge instead of the current.

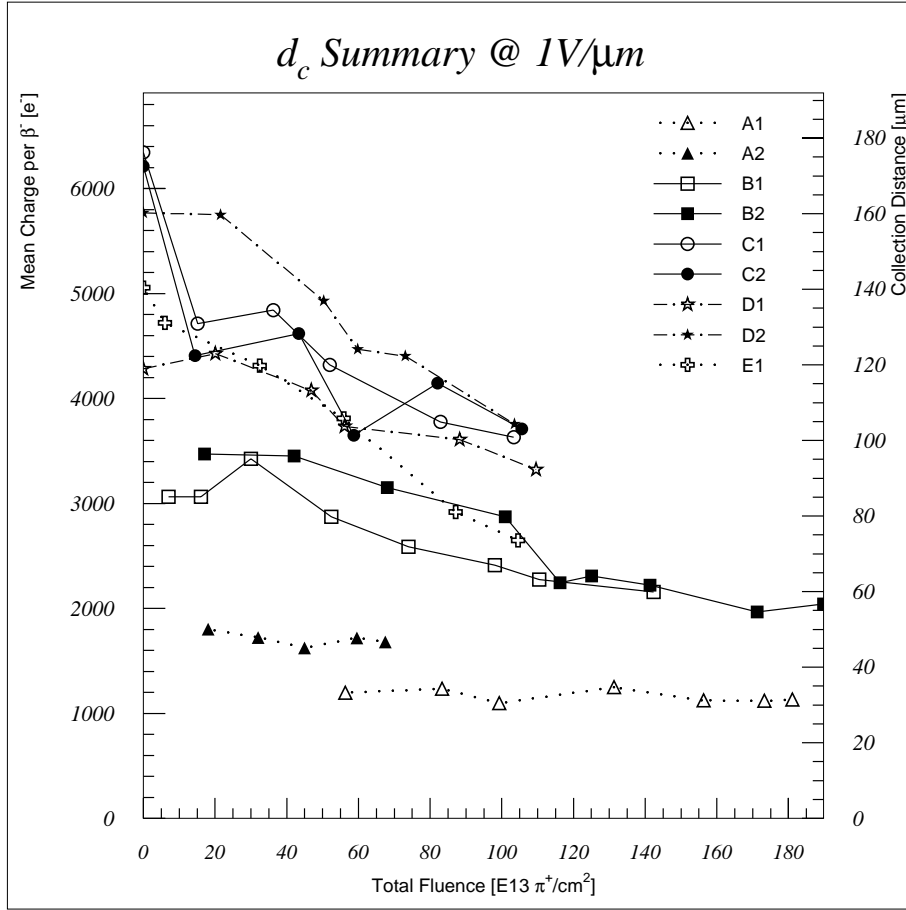


Figure 7.4: The charge collection distance of various samples vs. pion fluence.

By simple calculation, we can obtain the charge observed at the electrodes for a single traversing pion if we know the beam induced current (I_{ind}), the pion flux (ϕ_π) and the active area of the sample, which is bigger than the contact pad due to the fringe field (this will be discussed in detail in section 8.1). For the beam induced charge calculation, we will refer to this equivalent area (A_e), obtaining the equation

$$Q_c = \frac{I_{ind}}{\phi_\pi A_e} . \quad (7.1)$$

Using eq. 7.1, we can correlate the measured current of each sample with the number of electrons generated by a single traversing pion. It is very interesting to compare the beam induced charge with the collection distance measured with the ^{90}Sr source at the same bias voltage of 300 V. These two values should be identical for all fluences, but in fact they aren't. It turns out that the pion induced charge (pic) always exceeds the electron induced charge ($enic$).

We define the *excess factor* as the ratio $pic/enic$. Considering all samples, we observed excess factor curves within the shaded area of fig. 7.6. There are two components in the development of the excess factor vs. fluence. Easily seen at low fluences, there is

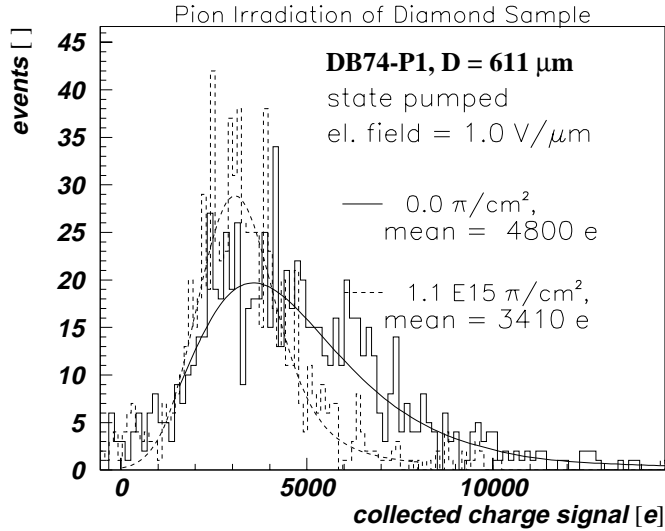


Figure 7.5: The pumped state signal distribution of a CVD diamond sample before and after receiving a pion fluence of 1.1×10^{15} particles cm^{-2} .

an exponential decay, and additionally, there is a constant factor of approximately 2, independent on the fluence. The reasons for the excess factor are currently unknown.

One irradiation experiment was performed each autumn from 1994 to 1997. It was found that the state of all samples was conserved over one year without irradiation, letting the *pic* continue at the end value of the previous year in all cases. During the intervals, the samples were characterized as well as pumped and depumped. Thus, for the excess factor, we can exclude short-term effects such as activation.

7.3.2 Electron Irradiation

In 1995, an irradiation was performed with 2.2 MeV electrons from a Van de Graaf accelerator at the Société AERIAL in Strasbourg, France [35]. The CVD diamond samples absorbed a fluence of up to 1 MGy (= 100 MRad), while no decrease in the charge collection distance could be observed, as shown in fig. 7.7.

7.3.3 Photon Irradiation

An irradiation experiment with 1.2 MeV photons emitted by a ^{60}Co source was carried out at the Argonne National Laboratory in 1993 [36]. The bias voltage during irradiation was resulting in an electric field strength of $0.2 \text{ V } \mu\text{m}^{-1}$.

In fig. 7.8, the collection distance is shown normalized to the unpumped value before irradiation vs. the photon fluence. The first four points were obtained with β electrons from a ^{90}Sr source and correspond to the pumping process, which saturates at a few 10 Gy.

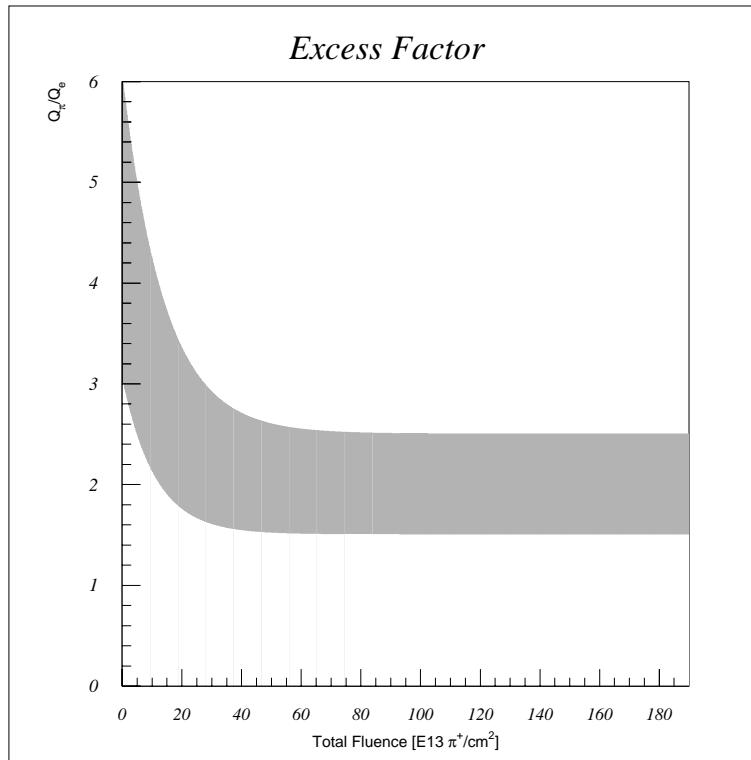


Figure 7.6: The range of the excess factor vs. fluence.

Up to 100 kGy of photon fluence, corresponding to 10 years of LHC operation at a radius of 20 cm from the vertex (see section 2), no change in the collected charge was observed.

7.3.4 Proton Irradiation

In 1997, diamond samples were irradiated at the PS at CERN [37] with protons. The momentum of the protons was $24 \text{ GeV } c^{-1}$. Another irradiation was performed earlier with $500 \text{ MeV } c^{-1}$ protons, showing compatible results.

Fig. 7.9 shows the development of the collection distance with proton fluence. After a fluence of $5 \times 10^{15} \text{ p cm}^{-2}$, exceeding by far the expected LHC fluence within 10 years at $r = 7 \text{ cm}$ from the vertex, the signal decrease is about 40%.

7.3.5 Neutron Irradiation

Diamond samples have been irradiated in 1995 at the ISIS facility at the Rutherford Appleton Laboratory with both thermal neutrons and neutrons with energy peaks at 10 keV and 1 MeV [15].

The pumping process and the neutron induced damage to the charge collection distance is shown in fig. 7.10. The charge collection distance normalization corresponds to the virgin unpumped state. The d_c decrease is approximately 20% after $10^{15} \text{ n cm}^{-2}$, which

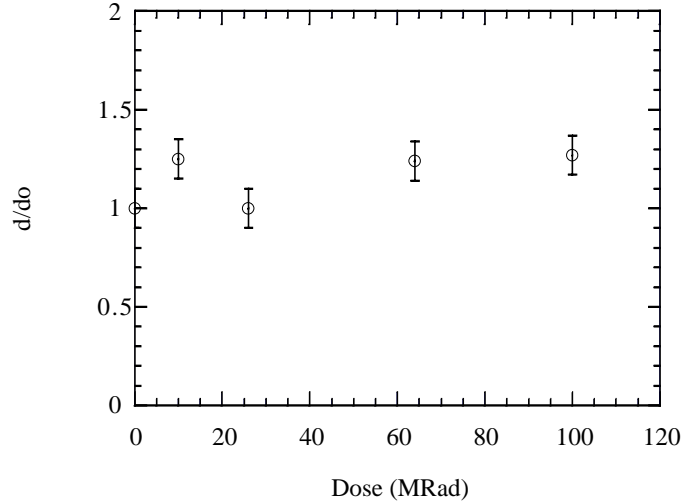


Figure 7.7: The d_c development with electron irradiation, normalized to the initial unpumped value. (100 MRad = 1 MGy)

corresponds to ten times the expected LHC fluence over 10 years at a radius of 7 cm from the vertex.

7.3.6 Alpha Irradiation

Some diamond samples were also exposed to an intense 5 MeV alpha beam at the Los Alamos National Laboratory [36]. The range of these particles in diamond is less than $15 \mu\text{m}$, thus affecting the surface region only. In order to measure the charge collection in this region, the two electrodes have been applied to the irradiated area on the same side of the diamond film. With this geometry, the electric drift field is restricted to the surface.

The charge collection distance normalized to the pumped value before irradiation is shown vs. the α fluence in fig. 7.11. The d_c decreases above a fluence of the order of $10^{12} \alpha \text{ cm}^{-2}$.

In contrast to the various types of particles mentioned in the previous sections, alpha radiation will not be significant at the LHC.

7.4 Comparison

Tab. 7.1 summarizes the collection distance damage introduced by hadronic particles. The d_c values are normalized to the pumped values before irradiation.

Among the hadronic particles, pions showed the worst effect on the charge collection distance. Comparing the nuclear interaction cross sections of protons and pions with protons (shown for pions in fig. 7.2), it turns out that the $300 \text{ MeV c}^{-1} \pi^+$ have an approximately five times higher cross section than 500 MeV c^{-1} or 24 GeV c^{-1} protons [38].

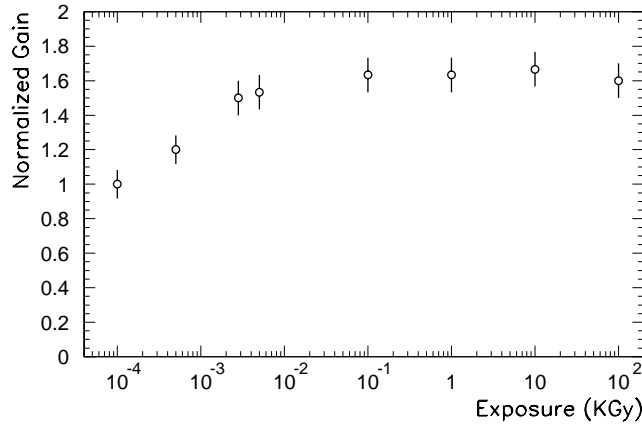


Figure 7.8: The d_c development with photon irradiation, normalized to the initial unpumped value.

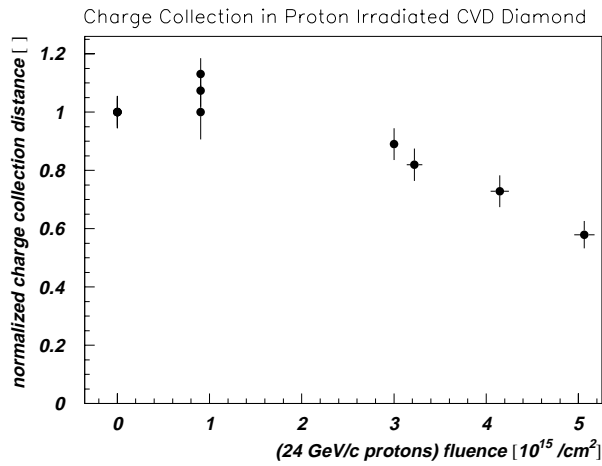


Figure 7.9: The charge collection distance vs. proton fluence, normalized to the initial pumped value.

This is in qualitative agreement with the observed d_c decrease.

A coarse estimation suggests that diamond detectors are technically feasible as tracking detectors up to a hadronic fluence of at least 10^{15} particles cm^{-2} , ten times more than present silicon detectors allow.

As discussed with the pion irradiation (section 7.3.1), diamond samples with higher initial collection distance are more affected by radiation than those of low quality. Furthermore, this also applies to regions of higher and lower local collection distance within a single sample. Thus, the irradiation has almost no effect on the rising edge of the Landau distribution. For the potential application as a detector with a certain trigger threshold at a few thousand electrons, the efficiency is less affected than suggested by the collection distance decrease.

Alpha particles are known to damage solid state detectors by a factor of 100 to 1000 more than minimum ionizing particles. The measured data agrees with this factor.

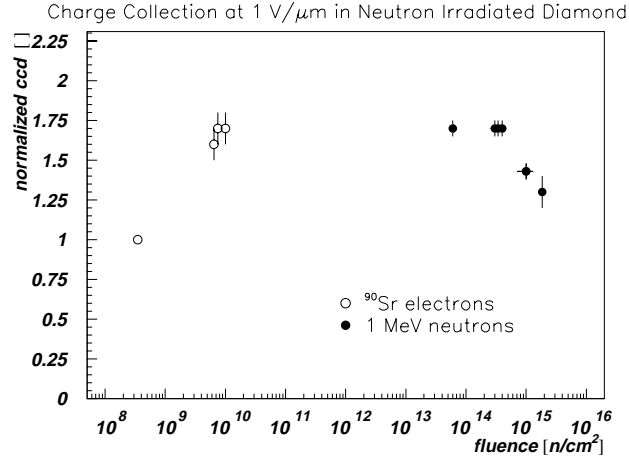


Figure 7.10: The development of the charge collection distance, normalized to the initial unpumped value, during the pumping process under a ^{90}Sr source and with neutron irradiation.

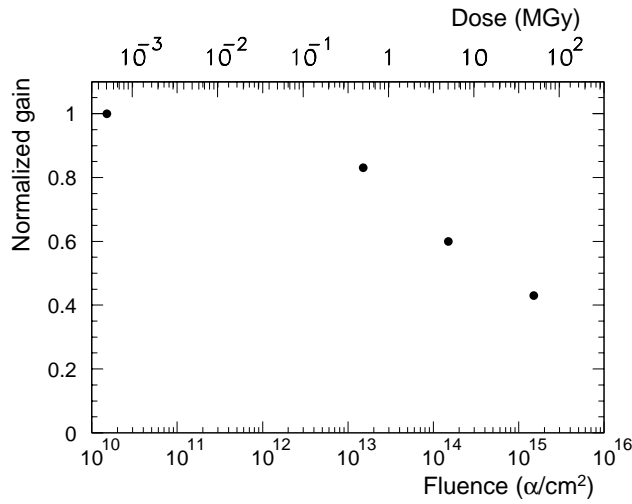


Figure 7.11: The d_c development with α irradiation.

Hadron	d_c/d_{c0} after	
	10^{15} cm^{-2}	$5 \times 10^{15} \text{ cm}^{-2}$
Proton	1	0.6
Pion	0.6	
Neutron	0.8	

Table 7.1: Normalized decrease of the charge collection distance after irradiation with different hadrons.

Chapter 8

Detector Geometries

Usually solid state tracking detectors have metal electrodes on opposite sides, however the geometric layout varies considerably. This has implications on the electric field distribution, the readout electronics and the spatial resolution.

8.1 Dots

In the simplest case, both electrodes are pads of equal size and shape at matching positions on either side. Thus, all induced charge from traversing particles is collected on the same electrode. In the diamond irradiation studies, the samples had circular pads with a diameter ranging from 1.8 to 5 mm. Although CVD diamond shows lateral inhomogeneities on a sub-millimeter scale, a pad area of 2.5 mm^2 and more is large enough to average over the fluctuations.

As long as the particle track is close to the pad center, the charge is generated in a homogeneous electric field, and the charge movement agrees with the model. Once the track hits the pad fringe, the electric field is no longer homogeneous.

For the diamond samples involved in the pion irradiation, the electric fringe field has been numerically calculated and the mean field strength has been computed on small ring elements. Together with the corresponding charge vs. electric field plots (fig. 5.4), the charge induced by hits in the area of the fringe field could be obtained. Finally, the actual electric field can be equivalently described by a sharp-edged homogeneous field 40 to 70% bigger than the pad area, depending on the sample geometry. However, as the charges follow the electric field, they have to cross more grain boundaries in the fringe region than in the homogeneous part. This could to some extent reduce the resulting charge and thus the equivalent area, but has been neglected in these calculations.

To avoid these complications, the samples can be equipped with a grounded guard ring electrode around the pad connected to the HV in order to restrict the fringe field. The simple dot and guard ring configurations are shown in fig. 8.1. This photograph also shows the different appearances of the smooth substrate side and the rough growth side.

Fig. 8.2 shows the electric field in a radial cross-section of a diamond sample ($D = 641 \mu\text{m}$) at 300 V bias without (a) and with (b) a guard ring. The borders of the shaded

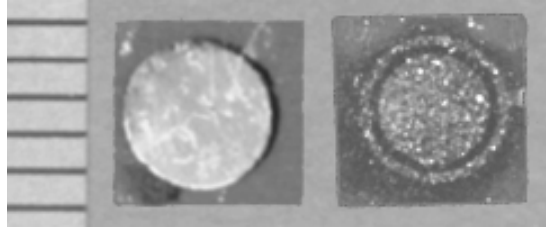


Figure 8.1: CVD diamond samples with a simple dot (substrate side) and with a guard ring (growth side). The scale ticks to the left represent millimeters.

areas are the equilines of potential (each shade corresponds to a 15 V interval), while the arrows show the negative gradient of the potential, i.e., the electric field. In total, the fringe field is significantly reduced by the guard structure, being restricted basically to a small range between the top and guard electrodes. Furthermore, the charges drained by the guard ring do no longer contribute to the signal, which is measured at the bottom electrode.

Guard rings are also used for silicon detectors, however, the reason there is primarily to reduce surface leakage currents.

8.2 Strips

Strip detectors have a large number of narrow strip implants on one side, while the opposite side is provided with a single, large electrode, called backplane. Normally, each of these strips is wire-bonded to a separate amplifier channel, allowing to detect the track position in one dimension. In some detector designs, only every second (or even third) strip is connected to an amplifier, while the remaining “intermediate strips” are terminated with high impedance. As there is a capacitive coupling, signals on these intermediate strips are partially transferred to the readout strips. With proper geometric design, the number of readout channels can be dramatically reduced while only little SNR is sacrificed. Strip and pixel detectors are often referred to as “trackers”, as their intention is the track reconstruction.

8.2.1 Spatial Resolution

The principal idea of not simply applying dots on both sides is to gain position information. At the cost of more amplifier channels and more complicated readout, the spatial resolution gets better with smaller electrode areas, forming strips or pixels. With a strip detector, the simplest case of data processing is to reduce the position information to the readout channel with the highest observed signal. Thus, the position information is digitized in steps of the strip pitch¹ p . Similar to the intrinsic noise of an ADC, one gets

¹distance from one strip center to the neighbor strip center

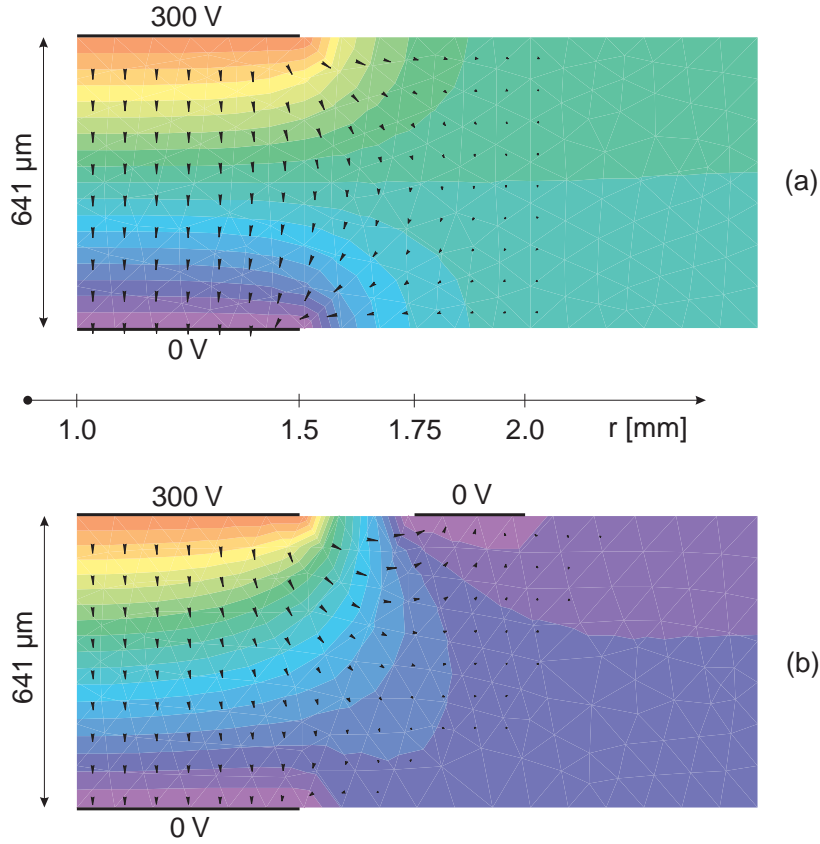


Figure 8.2: Cross-section of a diamond sample, showing potentials and the electric field without (a) and with (b) a grounded guard ring.

the digital (or, binary) resolution RMS of

$$RMS_{dr} = \frac{p}{\sqrt{12}} \quad . \quad (8.1)$$

When the strip pitch is small enough, charge sharing between two or more electrodes occurs, and together with proper analysis tools, the particle track can be reconstructed with much higher resolution than digital, depending primarily on the SNR. Using a silicon detector (300 μm thick) with a strip pitch of $p = 50 \mu\text{m}$ and a high-quality amplifier (e.g., the VA2), it is easy to obtain a spatial resolution of a few micrometers.

8.2.2 Measurements

When a diamond strip detector is measured in a test beam, the particle track is monitored with a number of high-resolution silicon strip reference detectors. Half of the reference detectors are rotated by 90° in order to obtain x and y position information. A system of such detectors, shown in fig. 8.3, is called “beam telescope”. The RD42 telescope utilizes 8 planes of silicon strip detectors with a pitch of 50 μm, which are read out by VA2 chips. The intrinsic resolution of this telescope is approximately 1.5 μm.

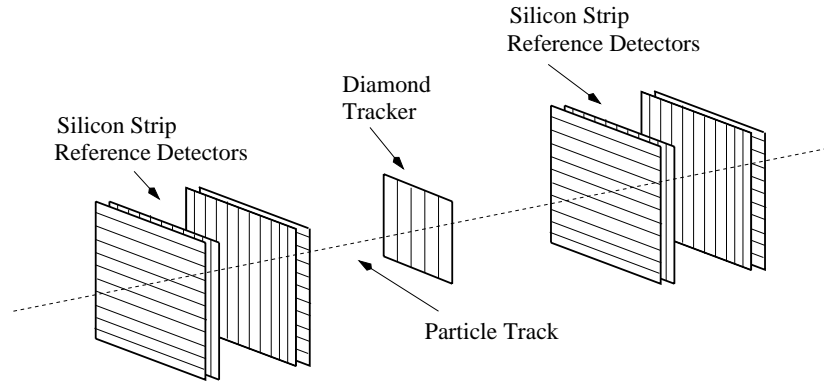


Figure 8.3: The RD42 beam telescope with a diamond tracker under test.

In the past years, several diamond samples have been equipped with strip electrodes and measured in test beams [22, 39]. The first diamond tracker, shown on the left side of fig. 8.4, was built and tested in 1994. It was made of a $1 \times 1 \text{ cm}^2$ piece of CVD diamond; the strips had a $100 \mu\text{m}$ pitch and a $50 \mu\text{m}$ interstrip gap. Using a VIKING readout chip, a mean SNR of 9 was achieved and the spatial resolution was $26 \mu\text{m}$, slightly better than the digital resolution ($29 \mu\text{m}$).

In the meantime, the quality of the CVD diamond material has been dramatically improved. Furthermore, as the intention was to achieve better spatial resolution, the strip pitch was reduced to $50 \mu\text{m}$. With the best diamond sample available, which has an area of $1 \times 1 \text{ cm}^2$, a mean SNR of 71 (most probable SNR=46) has been achieved with the VA2 readout chip. The measured spatial resolution of $\sigma = 15 \mu\text{m}$ approximately corresponds to the digital resolution for this strip pitch.

Recently, a $2 \times 4 \text{ cm}^2$ CVD diamond tracker with a pitch of $50 \mu\text{m}$ has been tested with VA2 amplifier chips (right side of fig. 8.4). With this configuration, a mean SNR of 30 and a spatial resolution of $14 \mu\text{m}$ has been obtained.

Apart from the slow, but low-noise VA2 chips, diamond strip detectors have also been tested with fast LHC front-end electronics. At the LHC, a bunch crossing occurs every 25 ns. In order to correlate the detector signal with a certain bunch crossing, the shaping time of the front-end electronics must be of the same order. Furthermore, the LHC amplifier chips need an analog pipeline storage, since the trigger decision, i.e., the request for event data, comes a few microseconds later. The SCT128AHC readout chip [40] has been designed for the ATLAS experiment, having a shaping time of 21 to 25 ns and a 128 cell analog pipeline. Due to the short integration time, the noise figure of this chip is $ENC \approx 650 \text{ e} + 70 \text{ e pF}^{-1}$, much higher than the noise of the VA2 chip.

The best available diamond detector, which was tested with the VA2 before, was later connected to the SCT128AHC readout chip without changing the strip pattern. This chip version is optimized for high capacitive load, i.e., silicon strip detectors, and thus not ideal for diamond detectors. Nevertheless, a mean SNR of 10 was demonstrated (most probable SNR=7.2) and a spatial resolution of $\sigma = 16.5 \mu\text{m}$ was observed.

Although the SNR figures of the same diamond strip detector measured with VA2 and SCT chips differ considerably, the spatial resolution is close to the digital resolution in

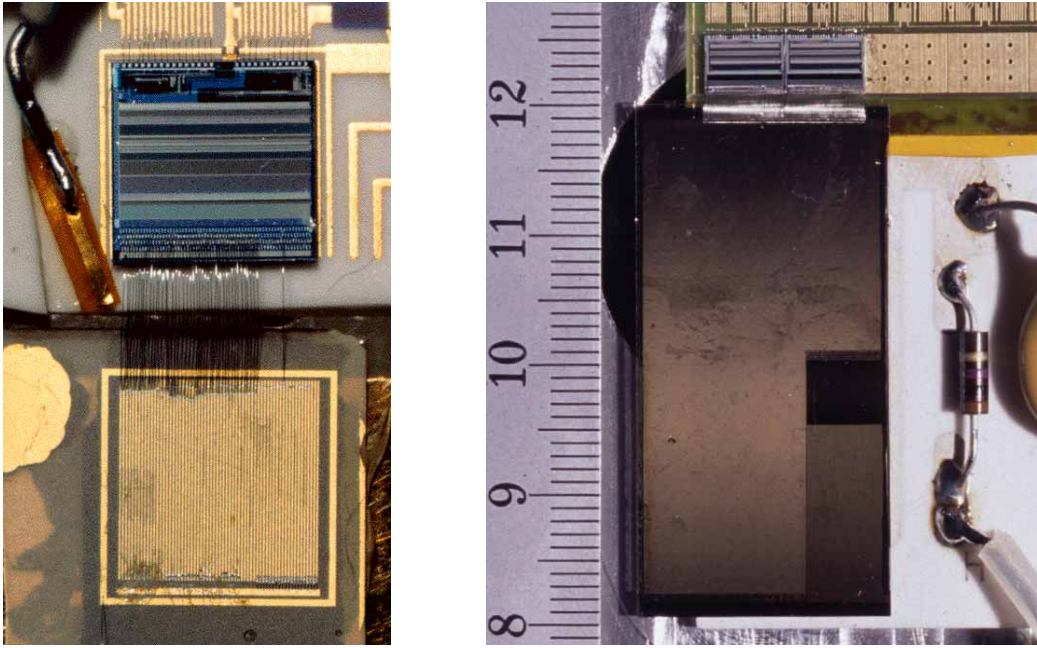


Figure 8.4: Left: The first CVD diamond tracker ($1 \times 1 \text{ cm}^2$) with a $100 \mu\text{m}$ pitch, wire-bonded to a VIKING readout chip. The strips are surrounded by a guard ring. Right: A $2 \times 4 \text{ cm}^2$ CVD diamond tracker, connected with two VA2 chips. The resistor and capacitor to the right form a low pass filter for the bias HV line; the scale's major ticks represent centimeters.

both cases. With silicon detectors, for comparison, the spatial resolution strongly depends on the SNR. It seems that certain limitations to the spatial resolution of CVD diamond are implied by the polycrystalline, inhomogeneous structure.

In order to obtain two-dimensional particle track information, two strip detectors can be used, one of which is rotated, as it is done in a beam telescope. However, this method is entirely secure only with low particle rates, i.e., one single particle per amplifier time constant, resulting in one hit strip in each plane. Otherwise, the hits may become ambiguous, and track reconstruction is no longer possible. One possible workaround to diminish the probability of such “ghosts” is to use a third strip layer under a certain angle. Theoretically, even more layers under different angles could be used, but the effort of track recognition would be far too complicated. The safe solution, at the cost of a large number of readout channels, is to use pixel detectors.

8.3 Pixels

A large number of small, equally shaped dots makes up a pixel detector. The dimensions of the pixels are primarily limited by the readout electronics. In contrast to strip detectors, here it is impossible to wire-bond the detector to a readout chip located nearby. Pixel detectors require a readout chip with amplifier cells of the same dimensions but mirrored, which is then bump-bonded onto the detector, forming a “sandwich”. This configuration

is shown in fig. 8.5.

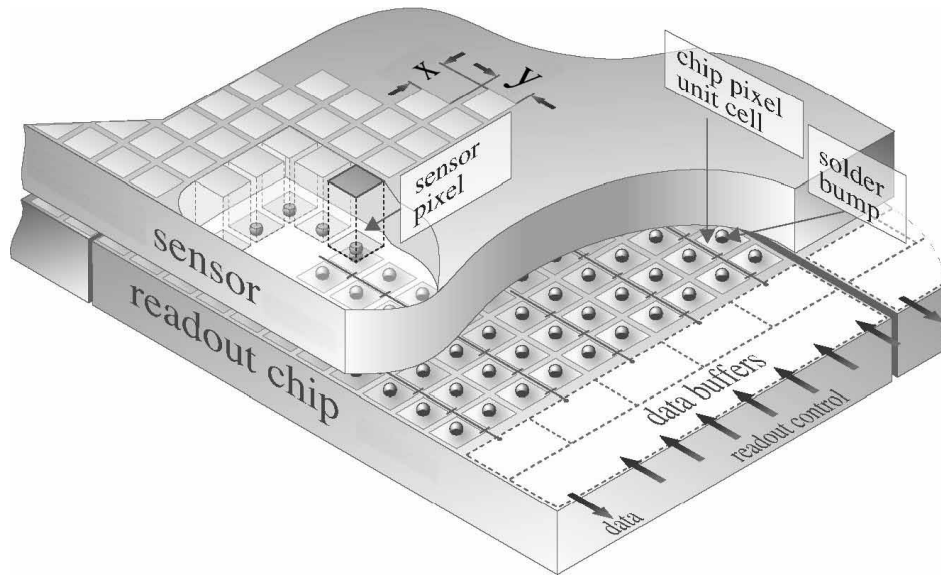


Figure 8.5: A pixel detector, bump-bonded onto the readout chip. x and y are the unit cell dimensions.

One method of bump-bonding will be described in brief. Each detector pixel metallization is passivated except for a small hole onto which indium is deposited from the vapor phase. After each pixel is prepared, the detector is heated until the indium forms a pearl on each pixel. Then the sample is pressed onto the readout chip, which is heated to 170°C . The intention is that each indium pearl forms a contact between a pixel and the corresponding readout cell.

Another type of pixel detector is the CCD (charge coupled device), which is primarily used for video and photographic purposes.

With the design of the CMS pixel detector for the LHC at CERN, a few CVD diamond samples have been prepared with $125 \times 125 \mu\text{m}^2$ pixels, as shown in fig. 8.6. The photograph to the right shows a close-up of individual pixel cells, where the indium pearls are visible.

Another pixel cell size is developed for the ATLAS pixel detector of the LHC. Here the cells are not square, but quite long and narrow. Fig. 8.7 shows the pixels cells, which measure $50 \times 536 \mu\text{m}^2$. The intention of the staggered layout is to improve the spatial resolution in the long dimension through charge sharing between adjacent pixels.

This pixel detector has been bump-bonded to the specifically designed readout chip, which complies with the LHC requirements. The system proved fully functional in a first test beam. Approximately digital resolution has been obtained in both dimensions in a preliminary analysis.

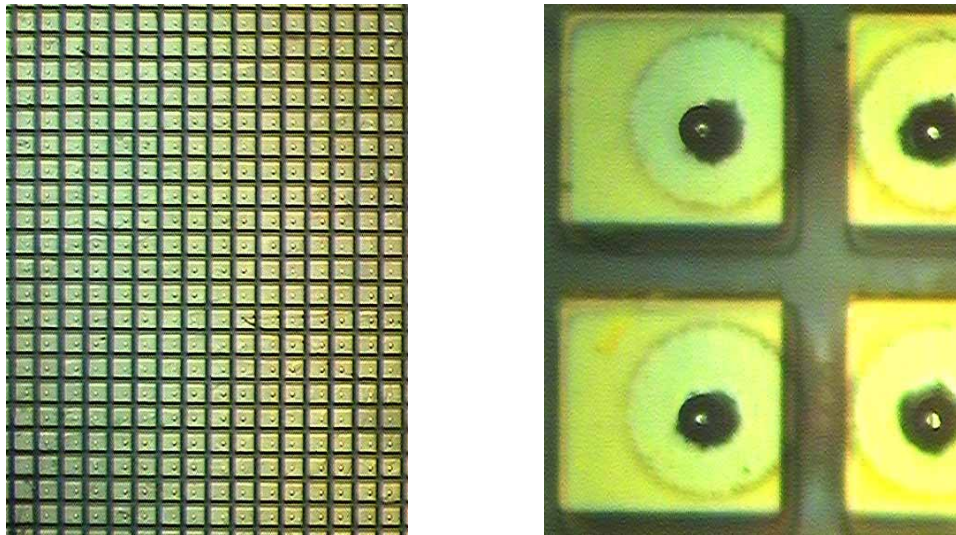


Figure 8.6: The CMS diamond pixel detector with $125 \times 125 \mu\text{m}^2$ unit cell size ($100 \times 100 \mu\text{m}^2$ electrodes). The indium pearls, which form the contact in the bump-bonding process, are visible in the close-up to the right.

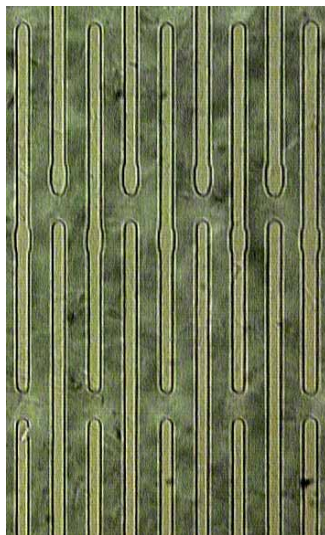


Figure 8.7: The ATLAS diamond pixel detector with $50 \times 536 \mu\text{m}^2$ cell size.

Chapter 9

Summary

The possible application of radiation detectors based on CVD diamond has been demonstrated. Similar to semiconductor detectors such as silicon, the Bethe-Bloch and Landau theories are efficient tools to describe the behavior of diamond detectors.

The polycrystalline structure of CVD diamond implies its inhomogeneity. A linear model over the detector thickness describes the relationship between local and average collection distances. This model satisfies experimental data. High quality CVD diamond is obtained by removing material with poor charge collection properties from the substrate side. The growth process has been successfully applied to grow large area detectors.

Excellent progress has been achieved over the past years by the RD42 collaboration. The charge collection distance of diamond has been increased, now reaching $230\ \mu\text{m}$ (corresponding to 8300 e) with a sample $432\ \mu\text{m}$ thick and slightly more with thicker samples. A compact characterization station was built in Vienna, which has been successfully used for pulse height measurements. Due to my contribution and optimization, it has a very low noise figure ($ENC = 270\ \text{e}$).

Moreover, I was involved in the pion irradiation of CVD diamond samples, which was carried out by the HEPHY in the autumns of 1995, 1996 and 1997. I made essential contributions in preparation, realization and data analysis including further studies such as the calculation of electric field distributions in diamond samples. In agreement with the linear model we could show that diamond samples with higher initial collection distance are more affected by irradiation than those with lower d_c . Similar, we have demonstrated that the upper (Landau) tail of the signal distribution suffers more from radiation than the low signal region, which remains almost unaffected. This implies that the efficiency of applications with a moderate threshold (a few thousand electrons) will be less affected by radiation than the mean value of the distribution.

Furthermore, the radiation hardness of diamond has been demonstrated for all major particles. Simplifying the results of the irradiation experiments, diamond is expected to survive a hadronic fluence of at least 10^{15} particles cm^{-2} , corresponding to the projected charged hadron fluence at a radius of 7cm from the vertex in the LHC accelerator at CERN over 10 years. This is ten times more than present silicon detectors allow.

Diamond micro-strip detectors were successfully tested with both slow (VA2) and fast (SCT128AHC) electronics. With the best diamond sample available, most probable

signal-to-noise ratios were observed to be 46 and 7.2, respectively, achieving approximately digital spatial resolution in both cases. However, the version of the SCT chip was not yet optimized for the small capacitive load of diamond detectors. The spatial resolution seems to be limited by the polycrystalline structure of CVD diamond. Furthermore, the first prototype of a diamond pixel detector (ATLAS design) demonstrated its functionality in a testbeam, and digital spatial resolution was observed in both dimensions.

The future program of RD42 includes further improvement of the charge collection distance as well as the growing of large area detectors. Emphasis will be laid upon the preparation and test of pixel detectors. Furthermore, the homogeneity studies will be continued to investigate the charge collection properties on a scale of a few tens of micrometers in the lateral dimension.

Acknowledgements

First of all, I am greatly indebted to my parents, who financed my university study and pushed me when I was somewhat lazy. Furthermore, I want to say thank you to my girlfriend Michaela. She was very patient when I was distressed with this work.

At the Institute of High Energy Physics, I primarily want to thank Prof. M. Regler, who offered me a job there after a laboratory course. This gave me the opportunity to learn a lot in the field of high energy physics and participate in the RD42 collaboration. Additionally, I am indebted to him for advising my diploma thesis. I am also indeed grateful to my mentors DI M. Pernicka, Dr. J. Hrubec and Dr. H. Pernegger for spending lots of their time with fruitful discussions. I owe special thanks to Doz. M. Krammer, not only for advising me whenever I had a question, but also for the effort of proofreading this thesis. I have always enjoyed the atmosphere of our group in the institute, and therefore I also want to thank all persons not mentioned.

Last, but not least, I owe many thanks to Prof. W. Fallmann for his effort of advising my diploma thesis.

Appendix A

Abbreviations and Symbols

The list below explains abbreviations used in this thesis.

Abbreviation	Meaning (explanation)
AC	Alternating current
ADC	Analog-to-digital converter
ATLAS	A toroidal LHC apparatus (LHC experiment)
CAMAC	(Standardized instrumentation for high energy physics, consisting of a crate and modules)
CCD	Charge coupled device (video pixel chip)
CERN	European Laboratory for Particle Physics, Geneva, CH
CMC	Common mode correction (method for removing shifts of all amplifier channels)
CMS	Compact Muon Solenoid (LHC experiment)
CVD	Chemical vapor deposition (growth process for diamond)
DC	Direct current
Fermilab	Fermi National Accelerator Laboratory, Batavia, USA
GSI	Gesellschaft für Schwerionenforschung, Darmstadt, D
HEPHY	Institute of High Energy Physics, Vienna, A [1]
HF	High frequency
HV	High voltage
LHC	Large Hadron Collider (future accelerator at CERN)
MIP	Minimum ionizing particle
OTA	Operational transconductance amplifier
ppm	Parts per million
PS	Proton Synchrotron (CERN accelerator)
PSI	Paul Scherrer Institute, Villigen, CH
RD42	Research & Development Programme 42 (diamond collaboration at CERN)

continued on next page

continued from previous page

Abbreviation	Meaning (explanation)
SEM	Scanning electron microscopy
SNR	Signal-to-noise ratio
SPS	Super Proton Synchrotron (CERN accelerator)
UV	Ultra-violet (light)

This list defines the symbols used for variables and constants.

Symbol	Definition	Units or Value
β	Speed relative to c	
$\delta(\gamma)$	Correction term	
ϵ	Relative dielectric constant	
ϵ_0	Dielectric constant	$8.85 \times 10^{-12} \text{ A s V}^{-1} \text{ m}^{-1}$
γ	$(1 - \beta^2)^{-1/2}$	
λ	Wavelength	nm
$\mu_{e,h}$	Electron, hole mobilities	$\text{cm}^2 \text{ V}^{-1} \text{ s}^{-1}$
ϕ	Flux	$\text{particles cm}^{-2} \text{ s}^{-1}$
ρ	Mass density	g cm^{-3}
ρ_c	Resistivity	$\Omega \text{ cm}$
σ	Standard deviation	<i>any unit</i>
σ_T	Thermal conductivity	$\text{W cm}^{-1} \text{ K}^{-1}$
$\tau_{e,h}$	Electron, hole lifetimes	s
A	Atomic mass	g mol^{-1}
	Amplifier gain	
A_e	Equivalent area	cm^2
a_F	Noise figure	dB
C	Capacitance	F
c	Speed of light in vacuum	$3.00 \times 10^{10} \text{ cm s}^{-1}$
C_{cal}	Calibration constant	e ADC^{-1}
cce	Charge collection efficiency	
D	Thickness of a diamond sample	cm
d_c	Charge collection distance	cm
dE/dx	Energy loss per unit length	eV cm^{-1}
E	Electric field strength	V cm^{-1}
	Energy	eV
e	Elementary charge	$1.60 \times 10^{-19} \text{ A s}$
	Base of the natural logarithm	2.72
E_g	Band gap	eV

continued on next page

continued from previous page

Symbol	Definition	Units or Value
E_{eh}	Energy to create e-h pair	eV
eic	Electron induced charge	e
ENC	Equivalent noise charge	e
f	Frequency	Hz
f_t	Transit frequency	Hz
flc	Fluence	particles cm^{-2}
h	Planck constant	6.63×10^{-34} J s
h_{fe}	Transistor DC gain	
I	Current	A
	Mean excitation energy	eV
k	Boltzmann constant	1.38×10^{-23} J K^{-1}
m_e	Electron mass	9.11×10^{-28} g
$m_{e,h}^*$	Electron, hole effective masses	g
N	Number of Atoms	cm^{-3}
n	Refraction index	
N_A	Avogadro's number	6.02×10^{23} mol^{-1}
n_i	Intrinsic carrier density	cm^{-3}
$N_{C,V}$	Conduction, valence band weights	cm^{-3}
p	Particle momentum	eV c^{-1}
	Strip pitch	cm
pic	Pion induced charge	e
Q	Charge	e
Q_c	Collected charge	e
Q_p	Generated charge	e
q_p	Mean MIP ionization	e cm^{-1}
r	Radius from the vertex	cm
	Voltage divider attenuation	
R	Resistance	Ω
r_e	Classical electron radius $\frac{e^2}{4\pi\epsilon_0 m_e c^2}$	2.82 fm
RMS	Root mean square	<i>any unit</i>
s	Laplace variable	
T	Absolute temperature	K
t	Time	s
T_{\max}	Maximum kinetic energy transfer	eV
T_p	Peaking time	s
v	Velocity	cm s^{-1}
V	Voltage	V
$v_{e,h}$	Electron, hole velocities	cm s^{-1}

continued on next page

continued from previous page

Symbol	Definition	Units or Value
X_0	Radiation length	cm
y	Distance from the substrate side	cm
Z	Atomic Number	
z	Distance from the vertex along the beam axis	cm
	Particle charge relative to e	

Appendix B

My Work with Diamonds

The following list states the diamond activities I was personally involved in.

Interval	Activity
Feb 1 - 24, 1995	Work on the VA2 readout at CERN
Mar 24, 1995 - Dec 20, 1996	Several contracts of work primarily devoted to diamond at HEPHY
Jul 9 - 29, 1995	Work on the characterization station at CERN
Aug 28 - Sep 6, 1995	Pion Irradiation at PSI
Sep 11 - Oct 10, 1996	Pion Irradiation at PSI
from Jan 7, 1997 on	Contract of employment partially devoted to diamond at HEPHY
Jan 21 - 22, 1997	RD42 collaboration meeting at CERN (talk)
May 12 - 13, 1997	RD42 collaboration meeting in Florence, I (talk)
Sep 22 - 23, 1997	ÖPG-Fachtagung Kern- und Teilchenphysik (Austrian Physical Society, section of Nuclear and Particle Physics) at Lindabrunn, A (talk)
Oct 2 - 3, 1997	RD42 collaboration meeting in Toronto, CAN (talk)
Nov 18 - Dec 2, 1997	Pion Irradiation at PSI
Feb 5 - 6, 1998	RD42 collaboration meeting in Amsterdam, NL (talk)
May 27 - 28, 1998	RD42 collaboration meeting at CERN (talk)
Sep 28 - Oct 4, 1998	7 th International Workshop on Vertex Detectors in Santorini, GR (talk and paper submitted to Nuclear Instruments and Methods in Physics Research A)

CERN: European Laboratory for Particle Physics, Geneva, CH (<http://www.cern.ch>)

HEPHY: Institute of High Energy Physics of the Austrian Academy of Sciences, Vienna, A (<http://wwwhephy.oeaw.ac.at>)

PSI: Paul Scherrer Institute, Villigen, CH (<http://www.psi.ch>)

Bibliography

- [1] Austrian Academy of Sciences, Institute of High Energy Physics, Nikolsdorfergasse 18, A-1050 Vienna, Austria (<http://wwwhephy.oeaw.ac.at>)
- [2] M. Krammer, private communication (Manfred.Krammer@cern.ch)
- [3] CMS Collaboration, **CMS Tracker Technical Design Report**, CERN/LHCC 98-6, April 1998
- [4] P. Moritz *et al.*, **Diamond Detectors for Beam Diagnostics in Heavy Ion Accelerators**, GSI-Preprint-97-64, October 1997
- [5] J. Conway *et al.*, **The Status of Diamond Detectors and a Proposal for R&D for CDF Beyond Run II**, CDF/DOC/TRACKING/PUBLIC/4233, July 1997
- [6] G. Davies (editor), **Properties and Growth of Diamond**, INSPEC, Institution of Electrical Engineers, London, 1994
- [7] L.S. Pan, D.R. Kania (editors), **Diamond: Electronic Properties and Applications**, Kluwer Academic Publishers, Boston/Dordrecht/London, 1995
- [8] S. Zhao, **Characterization of the Electrical Properties of Polycrystalline Diamond Films**, Ph.D. thesis, The Ohio State University, Columbus, 1994
- [9] I. Baumann, **Charakterisierung von Silizium-, Galliumarsenid- und Diamantdetektoren**, Dipoma Thesis, Max-Planck-Institut für Kernphysik, Heidelberg, 1996
- [10] E. Gatti, P.F. Manfredi, **Processing the Signals from Solid-State Detectors in Elementary-Particle Physics**, La Rivista del Nuovo Cimento della Società Italiana di Fisica, Vol. 9, N. 1, Bologna, 1986
- [11] St. Gobain/Norton Diamond Film, Goddard Road, Northboro, MA 01532, USA
- [12] De Beers Industrial Diamond Division Ltd., Charters, Sunninghill, Ascot, Berkshire, SL5 9PX England, UK
- [13] R.M. Barnett *et al.*, **Physical Review D54**, 1 (1996) and 1997 off-year partial update for the 1998 edition available on the PDG WWW pages (<http://pdg.lbl.gov>)

- [14] M. Regler, R. Frühwirth (editors), **Data Analysis Techniques for High-Energy Physics Experiments**, Second Edition, Cambridge University Press, Cambridge, 1999
- [15] D. Husson *et al.* (RD42 Collaboration), **Neutron Irradiation of CVD Diamond Samples for Tracking Detectors**, Nuclear Instruments and Methods in Physics Research A 388 (1997), 421-426
- [16] C. Grupen, **Teilchendetektoren**, B.I.-Wissenschaftsverlag, Mannheim/Leipzig/Wien/Zürich, 1993
- [17] M. Winkler, private communication (Matthias.Winkler@cern.ch)
- [18] L.D. Landau, **On the Energy Loss of Fast Particles by Ionisation**, Collected Papers of L.D. Landau, Pergamon Press, Oxford, 1965
- [19] J.E. Moyal, **Theory of Ionization Fluctuations**, Philosophical Magazine 46 (1955), 263-280
- [20] K.S. Kölbig, B. Schorr, **A Program Package for the Landau Distribution**, Computer Physics Communications 31 (1984), 97-111
- [21] K.S. Kölbig, **Landau Distribution**, CERN Computer Center Program Library G110 (<http://wwwinfo.cern.ch/asdoc/shortwrupsdir/g110/top.html>)
- [22] W. Adam *et al.* (RD42 Collaboration), **Development of Diamond Tracking Detectors for High Luminosity Experiments at the LHC**, CERN/LHCC 98-20, Status Report/RD42, June 1998
- [23] M. Mishina, **Induced Charge in Diamond**, RD42 Internal Note 13, March 1998
- [24] M.A. Plano *et al.*, **Thickness Dependence of the Electrical Characteristics of Chemical Vapor Deposited Diamond Films**, Applied Physics Letters 64 (2), January 1994, 193-195
- [25] D. Rakoczy, **Charakterisierung von Siliziumstreifendetektoren für den DELPHI Very Forward Tracker**, Diploma Thesis, Institut für Hochenergiephysik der Österreichischen Akademie der Wissenschaften, Wien, 1997
- [26] G.F. Knoll, **Radiation Detection and Measurement**, Wiley, New York, 1979
- [27] Nuclear Science References (NSR) database (<http://isotopes.lbl.gov/isotopes/vuensdf.html>)
- [28] W.R. Leo, **Techniques for Nuclear and Particle Physics Experiments**, Springer-Verlag, Berlin/Heidelberg/New York, 1987

- [29] A. Hrisoho, **Front-End Electronics for H.E.P.**, Proceedings of the III ICFA School on Instrumentation in Elementary Particle Physics, Rio de Janeiro, Brazil, July 1990, World Scientific, Singapore, 1992
- [30] IDE AS, Integrated Detectors & Electronics, Veritasveien 9, 1322 Høvik, Norway (<http://www.ideas.no>)
- [31] O. Toker *et al.*, **VIKING, a CMOS Low Noise Monolithic 128 Channel Frontend for Si-Strip Detector Readout**, Nuclear Instruments and Methods in Physics Research A 340 (1994), 572-579
- [32] E. Nygård *et al.*, **CMOS Low Noise Amplifier for Microstrip Readout Design and Results**, Nuclear Instruments and Methods in Physics Research A 301 (1991), 506-516
- [33] A. Rudge, **Comparison of Charge Collection in Semiconductor Detectors and Timing Resolution, Using a Sub-Nanosecond Transimpedance Amplifier**, Nuclear Instruments and Methods in Physics Research A 360 (1995), 169-176
- [34] M. Friedl *et al.* (RD42 Collaboration), **Pion Irradiation Studies of CVD Diamond Detectors**, RD42 Internal Note 12a, May 1998, to be submitted to Nuclear Instruments and Methods in Physics Research A
- [35] C. Bauer *et al.* (RD42 Collaboration), **Development of Diamond Tracking Detectors for High Luminosity Experiments at the LHC**, CERN/LHCC 95-43, LDRB Status Report, November 1995
- [36] C. Bauer *et al.* (RD42 Collaboration), **Radiation Hardness Studies of CVD Diamond Detectors**, Nuclear Instruments and Methods in Physics Research A 367 (1995), 207-211
- [37] D. Meier *et al.* (RD42 Collaboration), **Proton Irradiation Studies of CVD Diamond Detectors**, June 1998, submitted to Nuclear Instruments and Methods in Physics Research A
- [38] D. Meier, **CVD Diamond Irradiations with Protons and Pions**, Minutes of the RD42 Meeting 02/98, Amsterdam, February 1998
- [39] F. Borchelt *et al.* (RD42 Collaboration), **First Measurements with a Diamond Microstrip Detector**, Nuclear Instruments and Methods in Physics Research A 354 (1995), 318-327
- [40] F. Anghinolfi *et al.*, **SCTA - A Radiation Hard BiCMOS Analogue Readout ASIC for the ATLAS Semiconductor Tracker**, IEEE Transactions on Nuclear Science 44 (1997), 298-302